# Forest Fire Aerosol – Weather Feedbacks over Western North America Using a High-Resolution, On-line Coupled, Air-Quality Model

Paul A. Makar[1], Ayodeji Akingunola[1], Jack Chen[1], Balbir Pabla[1], Wanmin Gong[1], Craig Stroud[1], Christopher Sioris[1], Kerry Anderson[2], Philip Cheung[1], Junhua Zhang[1], Jason Milbrandt[3]

[1]Air Quality Research Division, Atmospheric Science and Technology Directorate, Environment and Climate Change Canada, 4905 Dufferin Street, Toronto, M3H 5T4, Canada
[2]Natural Resources Canada (emiritus), Summerland, British Columbia, Canada.
[3]Meteorological Research Division, Atmospheric Science and Technology Directorate, Environment and Climate Change Canada, 2121 Trans Canada Highway, Montreal, Canada

*Correspondence to*: Paul A. Makar (paul.makar@canada.ca)

**Abstract.** The influence of both anthropogenic and forest fire emissions, and their and subsequent chemical and physical processing, on the accuracy of weather and air-quality forecasts, was studied using a high resolution, on-line coupled air-quality model. Simulations were carried out for the period 4 July through 5 August 2019, at 2.5-km horizontal grid cell size, over a 2250 x 3425 km$^2$ domain covering western Canada and USA, prior to the use of the forecast system as part of the FIREX-AQ ensemble forecast. Several large forest fires took place in the Canadian portion of the domain during the study period. A feature of the implementation was the incorporation of a new on-line version of the Canadian Forest Fire Emissions Prediction System (CFFEPSv4.0). This inclusion of thermodynamic forest fire plume-rise calculations directly into the on-line air-quality model allowed us to simulate the interactions between forest fire plume development and weather. Incorporating feedbacks resulted in weather forecast performance that exceeded or matched the no-feedback forecast, at greater than 90% confidence, at most times and heights in the atmosphere. The feedback forecast out-performed the feedback forecast at 35 out of 48 statistical evaluation scores, for PM2.5, NO$_2$ and O$_3$. Relative to the climatological cloud condensation nuclei and aerosol optical properties used in the no-feedback simulations, the on-line coupled model's aerosol indirect and direct effects were shown to result in feedback loops characterized by decreased surface temperatures in regions affected by forest fire plumes, decreases in stability within the smoke plume, increases in stability further aloft, and increased lower troposphere cloud droplet and raindrop number densities. The aerosol direct and indirect effect reduced oceanic cloud droplet number densities and increased oceanic rain drop number densities, relative to the no-feedback climatological simulation. The aerosol direct and indirect effects were responsible for changes to the near-surface PM2.5 and NO$_2$ concentrations at greater than the 90% confidence level near the forest fires, with O$_3$ changes remaining below the 90% confidence level. The simulations show that incorporating aerosol direct and indirect effect feedbacks can significantly improve the accuracy of weather and air quality forecasts, and that forest fire plume rise calculations within a on-line coupled model changes the

32  predicted fire plume dispersion and emissions, the latter through changing the meteorology driving fire intensity and fuel

33  consumption.


## 1 Introduction

35  Atmospheric aerosol particles may be emitted (primary particles) or result from the condensation of the products of gas-phase

36  oxidation reactions (secondary aerosol). With increasing transport time from emission sources, the processes of coagulation

37  (colliding particles stick adhere creating larger particles) and condensation (low volatility gases condense to particle surfaces)

38  tend to result in particles which have a greater degree of internal mixing (internal homogeneous mixtures). Primary and near-

39  source particles are more likely to have a single or a smaller number of chemical constituents (external mixtures).

40  Atmospheric particles also modify weather through well-established pathways. Under clear sky conditions, the particles may

41  absorb and/or scatter incoming light, depending on their size, shape, mixing state (internal, external or combinations) and their

42  composition. The presence of the particles themselves may thus affect the radiative budget of the atmosphere, resulting in

43  either positive or negative climate forcing (i.e. the absorption of a greater amount of incoming solar radiation versus increased

44  scattering reflection of that radiation back out into space, a process known as the Aerosol Direct Effect; ADE). Aerosols can

45  also alter the atmospheric radiative balance through interactions with clouds, this influence being referred to as the Aerosol

46  Indirect Effect (AIE). Three broad classes of categories by which cloud/aerosol interactions take place (Oreopoulos *et al.,*

47  2020) include the first indirect effect, where higher aerosol loadings resulting in increasing numbers of cloud droplets with

48  smaller sizes, hence increasing cloud albedo (Twomey *et al.,* 1977), the second indirect effect, where higher aerosol loadings

49  suppress the collision-coalescence activity of the smaller droplets, reducing precipitation/drizzle, changing cloud heights, and

50  changing cloud lifetime in warm clouds (Albrecht, 1989), and aerosol "invigoration" of storm clouds, where higher aerosol

51  loadings may result in delayed glaciation of cloud droplets, in turn leading to greater latent heat release and stronger convection

52  (Rosenfeld *et al.,* 2018).

53  The uncertainties associated with the ADE and particularly AIE account for a large portion of the uncertainties in current

54  climate model predictions for radiative forcing between 1750 and 2011 (Mhyre *et al.,* 2013). Carbon dioxide is believed to

55  have a positive (warming) global radiative forcing of approximately 1.88 +/- 0.20 $Wm^{-2}$, while the direct and indirect effects

56  both have nominal values of approximately -0.45 $Wm^{-2}$, with uncertainty ranges encompassing -0.94 to +0.07 and -1.22 to 0.0

57  $Wm^{-2}$ respectively. These uncertainties have spurred research designed to better characterize the ADE and AIE, and reduce

58  these uncertainties, through both observations and atmospheric modelling.

59  Observational studies of the ADE have established its large impact; for example, high aerosol loading over Eurasian boreal

60  forests has been found to double the diffuse fraction of global radiation (i.e. increased scattering), a change sufficient to affect

61  plant growth characterized via gross primary production (Ezhova *et al.,* 2018). Aerosol assimilation of Geostationary Ocean

62  Color Imager Aerosol Optical Depth (AOD) observations into a coupled meteorology-chemistry model showed that South

63  Korean AOD values increased by as much as 0.15 with the use of assimilation; these increases corresponded to a local -31.39

W m$^{-2}$ reduction in solar radiation received at the surface, and reductions in planetary boundary layer height, air temperature, and surface wind speed over land, and a deceleration of vertical transport (Jung *et al.,* 2019). Other studies in East Asia have shown ADE decreasing local shortwave reaching the surface by -20 W m$^{-2}$ (Wang *et al.,* 2016), as well as significant changes in surface particulate matter and gas concentrations in response to these radiation changes.

However, one commonality amongst the recent studies of the ADE for air-quality models is a tendency towards negative biases in predicted aerosol optical depths, potentially indicating systematic under-predictions in aerosol mass, aerosol size, and/or inaccuracies in the assumptions for shape and/or mixing state. Mallet *et al. (*2017) noted this negative bias for regional climate model AOD predictions associated with large California forest fires compared to OMI and MRIS satellite observations. Palacios-Pena *et al. (*2018) noted that high AOD events associated with forest fires were under-predicted by most models in a study employing a multi-regional-model ensemble. The chosen AOD calculation methodology and mixing state assumptions employed in models also plays a role in systematic biases: Curci *et al. (*2015) compared aerosol optical depths, single scattering albedos, and asymmetry factors at different locations to observations, varying the source model for the aerosol composition, as well as the mixing state assumptions used in generating aerosol optical properties, for Europe and North America. AODs were biased low by a factor of two or more, regardless of model aerosol inputs or mixing state assumptions at 440 nm, single scattering albedos were biased low by up to a factor of two, with the poorest performance for "core-shell" approaches, while asymmetry factor estimates showed no consistent bias relative to observations. However, the assumed mixing state was clearly a controlling factor in the negative biases; the AOD predictions closest to the observations at 440 nm assumed an external mixture with particle sulphate and nitrate assumed to grow hygroscopically as pure sulphuric acid, lowering their refractive index with increasing aerosol size. This mixing state assumption and the different homogeneous mixture assumptions gave the best fit for single scattering albedo relative to observations. While not commenting on aerosol direct effect implications, Takeishi *et al. (*2020) noted that forest fire aerosols increase particle number concentrations but reduce their water uptake (hygroscopicity) relative to anthropogenic aerosols, with the latter effect reducing the resulting cloud droplet numbers by up to 37%. Mixing state and hygroscopicity properties of aerosols were thus shown to have a controlling influence on the ADE. The AIE has often been shown to be locally more important for the radiative balance than ADE in terms of magnitude of the radiative forcing and response of predicted weather to AIE and ADE (Makar *et al.,* 2015(a); Jiang *et al.,* 2015; Nazarenko *et al.,* 2017). Several recent studies have attempted to characterize the relative importance of the AIE with the use of multi-year satellite observations, sometimes making use of models and data assimilation. Saponaro *et al. (*2017) used MODIS/Aqua linked observations of aerosol optical depth and Ångström exponent to various cloud properties, noting that the cloud fraction, cloud optical thickness, liquid water path, and cloud top height all increased with increasing aerosol loading, while cloud droplet effective radius decreased, with the effects dominating at low levels (between 900 to 700 hPa). Zhao *et al.* (2018) examined 30 years of cloud and aerosol data (1981-2011), and found that increasing aerosol loading up to AOD < 0.08 increased cloud cover fraction and cloud top height, while further increases in aerosol loading (AOD from 0.08 to 0.13) resulted in higher cloud tops, and larger cloud droplets. In polluted environments (AOD > 0.30) cloud droplet effective radius, optical depth and water path; cloud droplet effective radius increased with increasing AOD. The first ADE was most sensitive

98    to AOD in the AOD range 0.13 to 0.30; and the reduction of precipitation efficiency associated with the second aerosol indirect

99    effect occurred for AODs between 0.08 and 0.4, in oceanic areas downwind of continental sources.

100   However, sources of uncertainty in AIE estimates persist, in part due to the number of poorly understood processes contributing

101   to the atmospheric response to the presence of aerosols. Nazerenko *et al.* (2017) showed that short-term atmospheric radiative

102   changes were reduced in magnitude when sea-surface temperature and sea-ice coupling was included in climate change

103   simulations. Suzuki *et al.* (2019) showed that the vertical structure of atmospheric aerosols, as well as their composition, had

104   a significant influence on radiative forcing. Penner *et al.* (2018) and Zhu *et al.* (2020) examined the impact of aerosol

105   composition on cirrus clouds via ice nucleation, finding negative forcings for most forms of soot, but a contrary impact of

106   secondary organic aerosols. Rothenburg *et al.* (2018) noted that tests of aerosol activation schemes carried out under current

107   climate conditions had little variability, but had much greater variability for pre-industrial simulations, implying that the

108   available data for evaluation using current conditions may poorly constrain ADE and AIE parameterizations used in simulating

109   in past climates.

110   Forest fires are of key interest for improving the understanding and representation of ADE and AIE in models, due to the large

111   amount of aerosols released during these biomass burning events. Forest fire emissions and interactions with weather are also

112   of interest due to the expectation that the meteorological conditions resulting in forest fires may become more prevalent in the

113   future under climate change (Hoegh-Guldberg *et al.*, 2018). Observations of aerosol optical properties during long-range

114   transport events of North American forest fire plumes to Europe showed 500 nm AOD values of 0.7 to 1.2 over Norway, with

115   Ångström exponents exceeding 1.4 and absorbing angstrom exponents ranging from 1.0 to 1.25, along with single scattering

116   albedos greater than 0.9 at the surface and up to 0.99 in the column over these sites (Markowicz *et al.,* 2016). Biomass burning

117   was shown to have a specific set of optical properties relatively independent of fuel type for three different types of biomass

118   burning in China (cropland), Siberia (mixed forest) and California (needleleaf forest). The increase in upward radiative forcing

119   at the top of the atmosphere due to fires being linearly correlated to AOD (R from 0.48 to 0.68), with slopes covering a

120   relatively small range from 20 to 23 W m$^{-2}$ unit AOD$^{-1}$. O'Neill *et al.* (2001) showed that forest fires have a profound impact

121   on aerosol optical depth in western Canada, accounting for 80% of the summer AOD variability in that region, with a factor

122   of three increase in AOD levels from clear-sky to forest fire plume conditions. O'Neill *et al.* (2001)'s analysis of TOMS

123   AVHRR and GOES imagery suggested that forest fire aerosols increase in size with increasing downwind distance, due to

124   secondary aerosol aging and condensation chemistry. We note here that reanalyzing the data presented in O'Neill *et al.* (2001)

125   results in a linear relationship between fine mode particle effective radius ($r_{eff}$, μm) and the base 10 logarithm of distance from

126   the fires (D, km) of $r_{eff} = 0.0106\ log_{10}(D) + 0.1163, R^2 = 0.18$). Mallet *et al.* (2017) simulated AODs in the range 1 to 2

127   for biomass burning events, and also noted changes in direct radiative forcing at the top of the atmosphere from positive to

128   negative in both model results and simulations, with increasing downwind distance from the sources. Lu *et al.* (2017) carried

129   out simulations with 5-km horizontal grid spacings for the eastern Russia forest fires of 2002 assuming an internal mixture for

130   emitted aerosols with the WRF-CHEM model, and noted impacts on cloud formation for two different periods. The first period

131   was characterized by high cloud droplet and small ice nuclei numbers, where the fire plumes reduced cloud rain and snow

132    water content, large scale frontal system dynamics were altered by smoke, and precipitation was delayed by a day. The second

133    period was characterized by high numbers for cloud droplets and ice nuclei, where the fire plumes reduced rain water content,

134    increased snow water content, and precipitation locations changed locally across the simulation domain. Russian forest fire

135    simulations for 2010 with suites of on-line coupled air-quality models (Makar *et al.,* 2015; Palacios-Pena *et al.*, 2018; Baro *et*

136    *al.,* 2017) showed substantial local impacts, such as reductions in average downward shortwave radiation of up to 80 W m$^{-2}$ and

137    temperature of -0.8 °C (Makar *et al.,* 2015(a)).

138    Given the above developments in direct and indirect parameterizations, and the increasing amount of information available for

139    estimating forest fire emissions, the impact of forest fires on weather, in the context of weather forecasting, is worthy of

140    consideration. Air-quality model predictions of forest fire plumes have been provided to the public under operational forecast

141    conditions of time- and memory-space limited computer resources (e.g. Chen *et al.,* 2019; James *et al.,* 2018; Ahmadov *et al.,*

142    2019, Pan  *et al.,* 2017).  These simulations make use of satellite retrievals of forest fire hot-spots, climatological data on the

143    extent of area burned by land use type, databases of fuel type linked to emission factors, and an *a priori* weather forecast to

144    provide the meteorological inputs required to predict forest fire plume rise. The latter point is worthy of note in the context of

145    the direct and indirect feedback studies noted above – both climate and weather simulations with prescribed forest fire

146    emissions have consistently resulted in large perturbations of weather patterns in the vicinity of the forest fires.  However,

147    their approaches for predicting forest fire plume rise and fire intensity and fuel consumption in operational regional scale

148    forecasts up until now have relied on weather forecast information provided *a priori* and hence lacking those meteorological

149    feedback effects.

150    The connection of the ADE and AIE within a regional air-quality and weather forecast model context is referred to as

151    "coupling", with such a model being described in that body of literature as "on-line coupled" (Galmarini *et al.,* 2015)  or

152    "aerosol-aware" (Grell and Freitas, 2014). However, several researchers have examined aerosol-radiative coupling along with

153    *fire spread and growth* (as opposed to fire intensity and fuel consumption).  The latter work employs very high-resolution

154    forest fire spread and growth models, and due to their very high resolution, an additional level of coupling, that of interaction

155    of dynamic meteorology with the heat released by the fire, may be included.  However, the resolution requirements for these

156    models (and their need for a relatively small computational time step) constrains their application to a relatively small region.

157    A requirement for these approaches is the use of a very high resolution fire growth model imbedded within the air-quality

158    model.   At these resolutions, the simulated local-scale meteorology determines fire spread on the landscape, which in turn

159    modifies the temperature and wind fields, in turn affecting future fire spread. The seminal work on this topic was carried out

160    by Clark *et al.* (1996), and Linn *et al.* (2002).  More recent work includes the development of the WRF-FIRE model (Mandel

161    *et al.,* 2011; Coen *et al.,* 2013), with full chemistry added in the WRFSC model (Kochanski *et al*., 2016). Examples of the

162    resolution required for these models include inner domain resolutions of 444 m with an imbedded fire model mesh of 22.2 m

163    resolution, and a time step of 3.3 seconds (Kochanski *et al.,* 2016); 1.33 km with an imbedded fire model mesh of 67.7m, and

164    a time step of 2 seconds (Kochanski *et al*., 2019), and 222m, with a fire model mesh of 22m and a time step of 2 seconds

165    (Peace *et al*., 2015).  Kochanski *et al* (2016) also noted a 13 to 30 hour computational time requirement to run their high-

resolution modelling system. These modelling efforts allow for this additional level of coupling – but at the expense of additional computation time preventing, at the current state of supercomputer processing, their application on synoptic-scale forecast domains combined with a full gas chemistry and size-resolved multi-component particle chemistry representation. Here we explore the effects of fire emissions characterized by fire intensity and fuel consumption modelling on the aerosol direct and indirect effects over synoptic scale domain. Our coupling refers to that between the aerosols released by fires and other sources to meteorology through the ADE and AIE, with the resulting changes in meteorology in turn influencing fire intensity and fuel consumption,, in turn influencing plume rise, emissions height, and distribution, closing this feedback loop. We do not implement a very high resolution growth model, noting that this is impractical for operational forecasts at the current time, while showing that synoptic scale 2.5km simulations incorporating fire feedbacks may be carried out within an operational window with currently available supercomputers. As shown below, we find that a sufficiently substantial feedback between the aerosol direct and indirect effects can be discerned to change the vertical distribution of emitted pollutants.

A key consideration in parameterizing the AIE (via aerosol-cloud interaction) is the manner in which the cloud condensation process is represented in the meteorological component of the modelling system. In numerical weather prediction (NWP) models, clouds and precipitation are represented by a combination of physical parameterizations that are each targeted at a specific subset of moist processes. These include "implicit" (subgrid-scale) clouds generated by the boundary layer and the convection parameterization schemes (e.g Sundqvist, 1988), and "explicit" clouds from the grid-scale condensation scheme (Milbrandt and Yau, 2005(a,b), Morrison and Milbrandt, 2015, Milbrandt and Morrison, 2016). Depending on the model grid these "moist physics" schemes vary in their relative importance.

However, regardless of the horizontal grid cell size, the grid-scale condensation scheme plays a crucial role in atmospheric models, though to different degrees and using different methods, depending on the grid spacing and the corresponding relative contributions of the implicit schemes. A grid-scale condensation scheme will in general consist of the following three components: 1) a subgrid cloud fraction parameterization (CF, or cloud "macrophysics" scheme); 2) a microphysics scheme; and 3) a precipitation scheme (Jouan *et al.*, 2020). The cloud fraction (CF) is the percentage of the grid element that is covered by cloud (and is saturated), even though the grid-scale relative humidity may be less than 100%. The microphysics parameterization computes the bulk effects of a complex set of cloud microphysical processes. If precipitating hydrometeors are advected by the model dynamics, the precipitation is said to be *prognostic*; if precipitation is assumed to fall instantly to the surface upon production, it is considered *diagnostic*. The precipitation "scheme" is not a separate component per se, since it simply reflects the level of detail in the microphysics parameterization, but it is a useful concept to facilitate the comparison of different grid-scale condensation parameterizations.

With a wide range of grid cell sizes in current NWP models, there is a wide variety of types of condensation schemes and degrees of complexity in their various components. For example, cloud-resolving models (with grid spacing on the order of 1 km or less) have typically used detailed bulk microphysics schemes (BMSs), with prognostic precipitation, and no diagnostic or prognostic CF component (i.e. the CF is either 0 or 1). Large-scale global models use condensation parameterizations, sometimes referred to as "stratiform" cloud schemes, typically with much simpler microphysics and diagnostic precipitation,

but with more emphasis on the details of the CF. However, with continually increasing computer resources and decreasing grid spacing (both in research and operational prediction systems), the distinction between schemes designed for specific ranges of model resolutions is disappearing and condensation schemes are being designed or modified to be more versatile and usable across a wider range of model resolutions (e.g. Milbrandt and Morrison, 2016).

Aerosol-cloud interactions and feedback mechanisms are difficult to represent in grid-scale condensation schemes with very simple microphysics components. For example, to benefit from the predicted number concentrations of cloud condensation nuclei and ice nuclei, the microphysics needs to be double-moment (predicting both mass and number) for at least cloud droplets and ice crystals, respectively. Until recently, detailed BMSs were only used at cloud resolving scales, hence requiring these relatively high resolutions to be recommended in feedback modelling. In recent years, multi-moment BMSs have been used in operational NWP for model grid spacings of 2-4 km (e.g. Seity *et al*., 2010, Pinto *et al*., 2015, Milbrandt *et al*., 2016). Further, condensation schemes with detailed microphysics are starting to use non-binary CF components (e.g. Chosson *et al*., 2014, Jouan *et al.,* 2020), thereby allowing detailed microphysics to be used at larger scales, and hence allowing the same indirect feedback parameterizations to be used at multiple scales. Nevertheless, the expectation is that detailed parameterization will provide a more accurate representation of cloud formation at the near cloud-resolving scales, without the complicating aspect of a diagnostic CF, motivating the use of km-scale grid spacing for feedback studies.

The formation of secondary aerosols from complex chemical reactions are another key consideration in feedback forecast implementation, given the impact of aerosol composition on aerosol optical and cloud formation properties, as described above. In the sections which follow, we describe our high resolution, on-line coupled air-quality model with on-line forest fire plume rise calculations, which was created as part of the FIREX-AQ air-quality forecast ensemble (https://www.esrl.noaa.gov/csl/projects/firex-aq/), to address the following questions:

(1) Will a on-line coupled model of this nature provide improved forecasts of *both* weather and air-quality, using standard operational forecast evaluation tools, techniques and metrics of forecast confidence? That is, despite the uncertainties in the literature as described above, are these processes sufficiently well described in our model that their use results in a formal improvement in forecast accuracy?

(2) Are the changes in forest fire plume rise associated with implementing this process directly within a on-line coupled model sufficient to result in significant perturbations to weather predictions and to chemistry? What are these perturbations?

We employ our on-line coupled model with 2.5-km grid cell size domain covering most of western North America, and compare model results to surface meteorological and chemical observations, and to vertical column observations of temperature and aerosol optical depth (AOD), in order to quantitatively evaluate the effect of feedback coupling of the ADE and AIE on model performance. We then compare feedback and no-feedback simulations to show the impacts of the ADE and AIE feedbacks on cloud and other meteorological predictions, and on key air quality variables (particulate matter, nitrogen dioxide, and ozone). We begin our analysis with a description of our modelling platform.

## 2 Model Description

### 2.1 GEM-MACH

The Global Environmental Multiscale – Modelling Air-quality and CHemistry (GEM-MACH) model in its on-line coupled configuration has been described elsewhere (Makar *et al.,* 2015a,b; Gong *et al.,* 2015, 2016). The model combines the Environment and Climate Change Canada Global Environmental Multiscale weather numerical weather prediction model (GEM, Cote *et al.,*, 1998, Girard *et al.,* 2014) with gas and particle process representation using the on-line paradigm, with options for climatological versus full coupling between meteorology and chemistry. GEM-MACH's main processes for the two configurations employed here are described in Table 1.

Simulations were carried out with a 2.5-km horizontal grid cell spacing over a 900 x 1370 grid cell domain, covering most of western Canada and the USA (Figure 1). The meteorological boundary conditions for the simulation were a combination of 10-km resolution GEM forecasts updated hourly (themselves originating in data assimilation analyses of real-time weather information; Figure 1(a)), and 2.5-km GEM simulations (Figure 1(c)) employing, in the northern portion of this 2.5-km domain, the Canadian Land Data Assimilation System (Carrera *et al.,* 2015), to better simulate surface conditions. Both "feedback" and "no feedback" simulations were carried out on a 30-hour forecast cycle (Figure 2). Following the usual practice for weather forecasts, the analysis-driven meteorological forecasts at 10 km resolution were updated operationally every 24 hours at 12 UT (Figure 2(a)). These 10 km resolution weather forecasts were used to drive a 30-hour, 10-km resolution GEM-MACH forecast (Figure 1(b), Figure 2(b)), which employed ECMWF reanalysis data for North American chemical lateral conditions (Innes *et al.,* 2019). The 10-km resolution weather forecasts were also used to drive a 30-hour meteorology-only forecast at 2.5-km resolution on the high resolution domain (Figure 1(c), Figure 2(c)). The last 24 hours of the 10-km resolution GEM-MACH forecast was also used to provide chemical lateral boundary conditions for the 24-hour 2.5km on-line coupled GEM-MACH simulation (Figure 1(c), Figure 2(d)). The last 24 hours of the 2.5-km GEM simulation were used as meteorological initial and boundary conditions for the 24-hour 2.5-km on-line coupled GEM-MACH simulation (Figure 1(c), Figure 2(d)). The two stages of meteorology-only simulations were carried out to prevent chaotic drift from the observed meteorology, and to allow spin-up time for the cloud fields of that meteorology to reach equilibrium (6-hour timeframe). Chemical initial concentrations for each consecutive forecast within the 2.5- km GEM-MACH model domain were "rolled over" or "daisy-chained" between subsequent forecasts without chemical data assimilation. Forecast performance scores presented here are for the inner 2.5-km domain from this set of linked 24 forecast simulations, mimicking operational forecast conditions.

### 2.2 CFFEPS Version 4.0: On-line forest-fire plume rise calculations

In addition to the above algorithm improvements relative to GEM-MACH implementations, this model system setup has incorporated the first on-line calculation of forest-fire plume-rise by energy balance driven using on-line meteorology, in a new version of the Canadian Forest Fire Emissions Prediction System (CFFEPS). The algorithms of CFFEPSv2.03 are

264 described in detail and evaluated elsewhere (Chen *et al.,* 2019), but will be outlined briefly here, as well as subsequent

265 modifications to this forest fire emissions processing module.

266 CFFEPS combines near-real-time satellite detection of forest fire hotspots with national statistics of burn areas by Canadian

267 province and by specific fuel type across North America. CFFEPS assumes persistence fire growth in the subsequent 24- to

268 72-hour forecasts with hourly fuel consumed calculated (kg m$^{-2}$), based on GEM forecast meteorology and predicted fire

269 intensity and fuel consumption in grid cells representing fire locations. The modelled fire fuel consumption is then linked with

270 combustion-phase specific emission factors (g kg$^{-1}$) for fire specific emissions and chemical speciation. Fire energy associated

271 with the modelled combustion process is also estimated, and is used in conjunction with *a priori* forecasts of meteorology

272 within the column to determine plume rise. In its off-line/non-coupled configuration (Chen *et al*., 2019), CFFEPS carries out

273 residual buoyancy calculations at five preset pressure levels (surface, 850, 700, 500, 250 mb). CFFEPS predicts plume injection

274 heights, which are in turn used to redistribute the mass emissions below the plume top to the model hybrid levels. This

275 approach employed in CFFEPSv2.03 provided a substantial improvement in forecast accuracy relative to the previous approach

276 employing modified Briggs (Briggs, 1965, Pavlovic *et al.,* 2016) plume rise formulae in the offline GEM-MACH forecast

277 system (Chen *et al.,* 2019). A recent evaluation of the plume heights predicted by CFFEPS was carried out utilizing MISR

278 and TROPOMI satellite retrieval data (Griffin et al, 2020). Seventy cases studied using MISR data showed good agreement

279 between satellite and CFFEPS-predicted maximum and mean plume heights (maximum plume height observed versus

280 predicted values and standard deviations: 1.7$\pm$0.9 versus 2.0$\pm$1.0 km; mean plume height observed versus predicted: 1.3$\pm$0.6

281 versus 1.3$\pm$0.4 km). A larger number of case studied using TROPOMI data (671 in total) also showed a reasonable agreement,

282 with CFFEPS showing a small tendency to overpredict heights (maximum observed versus predicted plume heights 2.2$\pm$1.6

283 versus 2.5$\pm$1.2 km; mean observed versus predicted plume heights 0.7$\pm$0.5 versus 1.1$\pm$0.6 km).

284 However, other work has shown the substantial impact of large forest fires on regional weather (Makar *et al.,* 2015a; Palacios-

285 Pena *et al.,* 2018, Baro *et al.,* 2017), including changes to the surface radiative balance and atmospheric stability. These

286 findings imply that plume rise calculations employing an *a priori* weather forecast lacking the impact of fire plumes via the

287 ADE and AIE may not accurately predict the weather conditions critical to subsequent forest fire plume rise prediction. In

288 order to study this possibility, and to allow forest fire plumes to influence weather and hence subsequent fire spread/growth,

289 several changes were made to CFFEPS implementation, resulting in version 4.0 of CFFEPS, used here. The process flow

290 within CFFEPSv2.03 versus CFFEPSv4.0 are compared in Figure 3. The original C language CFFEPSv2.03 code was

291 converted to FORTRAN90, and following successful off-line comparisons to the original code, was then integrated as an on-

292 line subroutine package within GEM-MACH itself, with the near-real-time satellite hotspot data and location fuel parameters

293 being read into GEM-MACH directly (CFFEPSv4.0 is this new on-line package). A key advantage of the CFFEPSv4.0

294 subroutine integration within GEM-MACH is that the residual buoyancy calculations for plume injection heights are now

295 carried out over the model hybrid model layers, rather than the five coarse resolution, prescribed pressure levels of

296 CFFEPSv2.03, making complete use of GEM-MACH's detailed vertical structure. Additionally, CFFEPSv4.0 allows plume

297 rise calculations to be updated during model runtime. When GEM-MACH is run in on-line coupled mode, the ADE and AIE

implementations allow model-generated aerosols to modify the predicted meteorology, in turn influencing predicted fire emissions and plume rise, closing these feedback loops. The on-line implementation of CFFEPSv4.0 thus allows us to investigate the effects of meteorology on subsequent forest fire plume development, the changes to modelled aerosol compositions, and, ultimately, the feedbacks to weather.

The formation of particles from forest fires affects meteorology on the larger scale via the ADE and AIE, in turn modifying the regional scale atmospheric features affecting fire growth, such as the temperature profiles below forest fire plumes. However, we note that CFFEPSv4.0 employs forest fire heat to determine plume rise as a subgridscale thermodynamic process parameterization rather than a very high resolution explicit fire growth parameterization; the very local scale weather modifications due to the addition of forest fire heat to the atmosphere are not incorporated into fire spread or GEM microphysics. Specifically, when the feedback version of GEM-MACH incorporating CFFEPSv4.0 is used in its on-line coupled configuration, CFFEPSv4.0 uses estimates of the heat released to calculate forest fire plume rise. These calculations employ lapse rates at the fire locations, that with feedbacks enabled, include the ADE and AIE generated by forest fire aerosols on atmospheric stability within the current on-line coupled model timestep. This is in contrast to earlier off-line implementations of CFFEPS, which made use of *a priori* non-feedback weather forecast lapse rates. To the best of our knowledge, this is the first implementation of a dynamic forest fire plume injection height scheme incorporated into a on-line coupled high-resolution, operational air quality forecast modelling system. The impact of this feedback on both weather and air-quality can be substantial, as we show in the following sections.

The locations of the daily forest hotspots detected during the study period, and the corresponding magnitude of the daily PM2.5 emissions generated by CFFEPS for each hotspot are shown in Figure 4. Individual hotspots with the highest magnitude emissions are located in the state of Nevada (Figure 4(a), southern boxed region). However, the largest ensemble emissions from a suite of hotspots occurs in northern Alberta (Figure 4(a), northern boxed region). Expanded views of the northern Alberta and Nevada hotspots are shown in Figure 4(b,c) respectively – the use of smaller symbols shows that the Alberta hotspots are groups representing large spreading fires, which overplotted in Figure 4(a), while the Nevada hotspots indicate single fires of small spatial extent and duration rather than larger spreading fires. The Alberta fires are thus the most significant sources of forest fire emissions in the study domain for the period analyzed here.


## 2.2 Feedback and No-Feedback Simulations

Two simulations were carried out for the period July 4th through August 5th 2019; a "feedback" (ADE and AIE feedbacks enabled – on-line coupled model) and a "no-feedback" simulation (ADE and AIE make use of GEM's climatological aerosol radiative and CCN properties – the one-way coupled model). During this period, five large forest fires took place in the northern portion of the modelling domain. The two parallel combined meteorology and air-quality forecasts in the on-line coupled model with/without ADE and AIE coupling were evaluated for meteorological and air quality variables. Following

330 evaluation, the simulation mean values of hourly meteorological and chemical tracer predictions were compared to analyze
331 the impact of on-line coupled ADE and AIE feedbacks on both sets of fields.

## 3 Model Evaluation

### 3.1 Meteorology Evaluation

334 Surface meteorological conditions were evaluated at three-hour intervals from the start of both of the two sets of paired 24-
335 hour forecasts using standard metrics of weather forecast performance including mean bias (MB), mean absolute error (MAE),
336 root mean square error (RMSE), correlation coefficient (R) and standard deviation ($\sigma$). In all comparisons, a 90% percent
337 confidence level assuming a normal distribution was used to identify statistically different results between forecast simulations.
338 Note that 90% confidence levels are commonly used in meteorological forecast evaluation, with values of 80% to 85%
339 recommended (Pinson and Kariniotakis, 2004) and up to 90% used (Luig *et al.*, 2001) for variables such as wind speed, rather
340 than the 95% or 99% confidence levels in other fields, in recognition of the difficulties inherent in prognostic forecasts of the
341 chaotic weather system. Here, the confidence range formulation of Geer (2014) has been applied using a 90% confidence
342 level in model predictions, with the statistical measures considered different at the 90% confidence level when the 90%
343 confidence ranges do not overlap. The surface meteorological evaluations shown here only include those variables and metrics
344 where results were significantly different at the 90% confidence level.

345 Several model forecast output variables were evaluated and the surface variables showing statistically significant differences
346 relative to observations at the 90% confidence level included: 2 m temperature, surface pressure, 2 m dewpoint temperature,
347 10 m wind speed, sea-level pressure, and accumulated precipitation (the latter in 3 different metrics). The comparisons are
348 shown as time series in three-hourly intervals as a function of forecast hour prediction time forward from forecast hour 0, for
349 grid cells corresponding to measurement locations in Figures 5, 6, 7, 8, 9, 10, and 11 for each of these quantities, respectively.
350 Note that these statistics measure domain-wide performance, across all of the reporting stations within the model domain,
351 during the sequence of 24-hour forecasts comprising the simulation period. The duration of the time series in these comparison
352 figures is thus a function of the duration of the contributing forecasts.

353 Figure 5 shows an example analysis for surface temperature bias for the entire model domain. Figure 5(a) shows the average
354 model mean bias (MB) time series across all stations and all forecasts at the given forecast hours, while Figure 5(b) shows the
355 corresponding difference in the MB absolute values. The difference plot in Figure 5(b) shows the feedback – no-feedback
356 scores, such that scores below the zero line indicate superior performance of the feedback forecast, while those above the zero
357 line indicate superior performance of the no-feedback forecast. Here, the feedback forecast was statistically superior at forecast
358 hours 3, 6, 15, 18 and 24 at the 90% confidence level at these forecast hours, and both simulations were at par (differences
359 below the 90% confidence level) at hours 12 and 21, with the no-feedback forecast being superior at 90% confidence at hour
360 9. The feedback forecast thus has superior performance, at greater than 90% confidence, over half of the forecast hours

evaluated within the domain, equivalent performance at two hours (hours 12 and 21, both within 90% confidence limits), and inferior performance at one hour (hour 9), during the simulation period.

All of the metrics for which surface temperature forecast performance differed at the 90% confidence level are shown in Figure 6. In addition to MB, the scores for MAE, and RMSE showed superior forecast performance for the feedback relative to the no-feedback case at the 90% confidence level for hours 15 and 18, while the improvement for the correlation coefficient was only reached the 90% confidence level at hour 18.

The meteorological forecast performance metrics with statistically significant differences for surface pressure, dewpoint temperature, and sea-level pressure are shown in Figures 7, 8, and 9 respectively. The model performance differences in these three Figures show a similar pattern: a degradation in performance with the use of feedbacks at hour 3, with the differences between the two forecasts either dropping below the 90% confidence level, or the feedback forecast showing an improvement by hour 9, followed by several hours in which the feedback forecast has a superior performance, usually at greater than 90% confidence. The duration of this latter period varies between the metrics, from up to 18 hours for MAE for surface pressure (Figure 7(b)) to 3 hours for the correlation coefficient of dew-point temperature (Figure 8(d)).

The initial loss of performance for the feedback forecast may represent a form of "model spin-up" that may be unique to on-line coupled models, but may be affected or improved with further adjustments to the forecast cycling setup for the chemical species. As noted earlier (Figure 2), in order to prevent chaotic drift from observed meteorology, we made use of a 30-hour 2.5-km resolution analysis-driven weather forecast to update our on-line coupled model's initial meteorology at hour zero of each 24 hour forecast. The cloud fields provided as initial conditions at hour zero include observation analysis for the 6 hours prior to hour zero - these have reached a quasi-equilibrium in the high-resolution weather forecast (Figures 2(b,e)) by the time they are used as initial and boundary conditions in the on-line coupled model (Figure 2(c,f)). However, the on-line coupled model's *aerosol* fields at hour zero, used to initialize the subsequent forecast (Figure 2, dashed blue arrow), still reflect the locations of aerosol-cloud interactions in the previous on-line coupled simulation. The initial three to six hours of feedback forecast degradation represents the time required for the on-line coupled model to reach a new equilibrium consistent between both its aerosol and the cloud fields.

One possible solution for this model spin-up inconsistency would be to eliminate the intermediate driving 2.5-km meteorological simulation in favour of a longer 30-hour on-line coupled forecast with the first six hours removed as spin-up (i.e. extend the duration of steps (c) and (f) in Figure 2 to 30 hours, starting at UT hour 6). The duration of the forecast experiments carried out here was limited to 24 hours due to limited computational resources, and, more importantly, the operational requirement for an on-time forecast delivery for the purpose of the FIREX-AQ field campaign. The 24-hour forecast simulations carried out in Figure 2 (c,f) each required nearly 3 hours of supercomputer processing time; longer simulation periods were not possible within the operational window available for forecasting.

Model 10-m wind speed forecasts were also improved with the incorporation of feedbacks for hours 3 and 6, for all metrics (Figure 10). A decrease in MB performance at hours 21 and 24 can also be seen in this Figure.

12

394　Precipitation forecast performance from the two simulations varied depending on the metric chosen (Figure 11). The metrics

395　in this case were based on the number of coincident precipitation "events" versus "non-events" as shown in contingency Table

396　2.

397　The Heidke skill score { $HSS = 2(AD - BC)/[(A + C)(C + D) + (A + B)(B + D)]$ } measures the fractional improvement

398　of the forecast over the number correct by chance. The Frequency Bias { $FB = (A + B)/(A + C)$ } measures the frequency

399　of event over-forecasts (FB>1) versus event under-forecasts (FB<1).　The Equitable Threat score { $ETS =$

400　$(A - \tilde{A})/(A + C + B - \tilde{A})$, where $\tilde{A} = (A + B)(A + C)/(A + B + C + D)$} measures the observed and/or forecast events

401　that were correctly predicted. Following standard practice at Environment and Climate Change Canada, the HSS is used as a

402　measure of total precipitation accumulated over a 6-hour interval, with no lower limit on the amount of precipitation defining

403　an "event", while FB and ETS define precipitation "events" as being those with greater than 2mm/ 6 hours – consequently FB

404　and ETS have a smaller number of data points for comparison than HSS.

405　Figure 11 shows improvements to the on-line coupled precipitation forecast at the 90% confidence level were seen for the HSS

406　6-hour accumulated metric at hours 12 and 24, while the frequency bias index of 6-hour accumulated precipitation showed

407　degradation at hours 6 and improved performance at hour 12, and the equitable threat score of 6-hour accumulated precipitation

408　showed significant differences at 90% confidence between the two simulations. As is noted above, the latter two metrics

409　employed a minimum 6-hour precipitation threshold of 2 mm prior to comparisons (this is the reason for the reduced number

410　of points available for comparison in Figure 11(b,c) relative to Figure 11(a)). These findings suggest that the on-line coupled

411　model's improvements for total precipitation (Figure 11(a)) are the result of slightly improved performance for relatively light

412　precipitation events (< 2mm 6hr$^{-1}$)..

413　The amalgamated observations and model pairs of vertical temperature profile data from 39 radiosonde sites in western North

414　America are shown in Figures 12 and 13. Improvements in the forecasted temperature vertical profile with increasing forecast

415　time are evident at 250, 300, 400, 500, and 850 hPa in the 12th hour forecast, with degradations at 200 and 700 hPa (Figure

416　12). Improvements at 300, 925 and 1000 hPa may be seen in the 24th hour (Figure 13) forecast; it is also worth noting the

417　entire region at and below 300 hPa has improved temperature forecasts (mean values to the left of the vertical line), albeit not

418　always at >90% confidence. There are larger differences between the 1000 hPa forecasts, though these also have the least

419　number of contributing stations (i.e. only those located close to sea-level contribute to the lowest level temperature biases).

420　Other levels of the atmosphere showed no statistically significant change at the 90% confidence level in temperature profile

421　forecast performance with the use of feedbacks.

422　**3.2 Chemistry Evaluation**

423　Improvements to air quality model performance metrics have been a focus for research since the 1980's starting with dispersion

424　model evaluation (Fox, 1981), and the identification of mean bias and normalized mean square error as potentially useful

425　metrics to complement the Pearson correlation coefficient (Hanna, 1988). More recently, the Pearson correlation coefficient

426　has been noted as being capably of producing high values for relatively poor model results (Krause *et al.*, 2005), as well as

13

being unable to distinguish systematic model underestimation (Yu *et al.*, 2006), unable to provide information on whether data series have a similar magnitude and capable of providing a false sense of relationship where none exists due to outliers (Duveiller *et al.*, 2016) and clusters of model-observation pairs (Aggarwal and Ranganathan, 2016). More recently, model evaluation has focused on metrics which do not have the tendency to weight the higher magnitude values unduly (a particularly useful property with air-quality variables which may vary by several orders of magnitude), which are dimensionless (allowing a comparison across different evaluated variables), and which are bounded and symmetric (properties allowing comparisons to be made and equally valued across the entire range of possible concentrations; e.g. Yu *et al.* (2006)). Metrics such as the modified coefficient of efficiency (Legates and McCabe, 1999) and the more recent incarnations of the Index Of Agreement (Willmott *et al.*, 2012) are examples of the more recent metrics used for air-quality model evaluation. Here, we have made use of a range of metrics spanning the literature on this topic, with the understanding that the properties of different metrics vary, that no single metric provides a perfect means of evaluating model performance, and that a variety of metrics should be applied. The metrics used here span the variety that have appeared in the literature since the early 1980's, and include Factor of 2, Mean Bias, Mean Gross Error, Normalized Mean Gross Error, Correlation Coefficient, Root Mean Square Error, Coefficient of Efficiency, and Index of Agreement. The formulae for these metrics and a brief description of their relative advantages and disadvantages appears in Appendix A (Supplemental Information).

Both simulations' performance for ozone ($O_3$), nitrogen dioxide ($NO_2$) and particulate matter with diameters less than 2.5 μm (PM2.5) were evaluated using the above metrics, employing hourly AIRNOW data (USA: AQS network: https://www.epa.gov/aqs; Canada: NAPS network: http://maps-cartes.ec.gc.ca/rnspa-naps/data.aspx) and the *openair* package (Carslaw and Ropkins, 2012). The summary performance metric scores for the two simulations grouped, according to contributing measurement network, are shown in Table 3, with boldface values indicating the better score for the given simulation case. With respect to this table, we note that:

(a) The feedback simulation generally outperforms the no-feedback simulation (more bold-face scores in the "feedback" rows, for 35 out of 48 metric comparisons).

(b) Feedback forecast score improvements occurred were more noticeable for PM2.5 (usually first to second digit), followed by $O_3$, with the $NO_2$ scores often being the same for the first few digits.

(c) We note that the boundary conditions employed for our 2.5km simulations had a strong impact on model air-quality performance. As described above, these boundary conditions originated in a 10-km resolution simulation making use of ECMWF global reanalysis values on its own lateral boundaries. The magnitudes of the statistics of Table 3 may be compared to the magnitudes of the statistics from our initial ACPD submission (which made use of a MOZART 2009 reanalysis for chemical lateral boundary conditions for the 2.5km GEM-MACH domain); these earlier results are shown in the S.I., Table A2 The use of feedbacks had a similar relative impact on forecast performance (34 out of 48 statistics improving in the feedback forecast in the initial simulation, compared to 35 out of 48 statistics in the current work). However, the net impact of the ECMWF-driven 10-km GEM-MACH values being used for chemical lateral boundary

14

461 conditions, rather than the MOZART climatology, was a degradation of performance: comparing the equivalent entries
462 in Table 3 and Table A2, it can be seen that 71 out of 96 scores were better with the earlier use of the MOZART reanalysis.
463 As we show below, however, the revised boundary conditions led to improvements in model aerosol optical depth
464 performance relative to observations.

466 The impact of lateral boundary conditions on model predictions can be seen when comparing MODIS retrievals of aerosol
467 optical depth (AOD) with model predictions (Figure 14). AOD is a function of both the particle's abundance and optical
468 properties, integrated throughout the vertical column. However, direct comparisons between satellite and model-predicted
469 AOD values must be undertaken with some care, due to the nature of the satellite retrieval quality assurance and control
470 procedures, the motion of the orbiting spacecraft, and the scan time of the instrument. The manner in which AOD is calculated
471 introduces additional uncertainty due to the range of values which may be derived from the same aerosol speciation using
472 different methodologies (Curci *et al.,* 2015). For a polar-orbiting instrument such as MODIS, the time at which overpasses
473 occur varies with location, and valid satellite retrievals may not occur when the location being scanned is obscured by clouds.
474 Observed averages may be built up over multiple valid scans over time, but the number of valid scans contributing to the local
475 average at any given location will vary, due to the time and space variation in cloud cover. Here, individual valid Collection
476 6.1 MODIS/Aqua (MYD04_L2 AOD_550_Dark_Target_Deep_Blue_Combined) 10 km resolution 550 nm AODs were
477 matched in time and space to the nearest model 2.5-km grid cell and output frequency hour. Levy *et al.,* (2013) contains details
478 on the MODIS combined AOD product. No averaging was employed in our comparison (Figure 14); all satellite overpass
479 AOD pixels and matching model AOD pixels are shown.. Noting that the AOD colour scale is logarithmic, the model
480 simulation driven using the ECMWF + 10-km resolution GEM-MACH for boundary conditions (Figure 14(b)) is a much better
481 match to observations (Figure 14(a)) than the model simulation driven by MOZART climatological boundary conditions
482 (Figure 14(c)). The slope of the linear best fit line between all observation and model pairs in each case mirrors this finding,
483 with the original (MOZART climatology) boundary conditions having a slope of 0.15 and $R^2$ of 0.0382, and the revised
484 ECMWF + GEM-MACH 10-km boundary conditions having a slope of 0.56 and an $R^2$ of 0.067.

486 Previous work with CFFEPS by Chen *et al. (*2019) for the 2017 fire season has shown similar $PM_{2.5}$ positive biases for western
487 Canada, with MB of +5.8 µg m$^{-3}$ (88 stations) and for Western USA with MB of +8.6 µg m$^{-3}$ (221 stations). These positive
488 biases (Chen *et al.,* 2019) were higher specific to sub-regions closer to areas of active fires (MB of +12 µg m$^{-3}$ for the sub-
489 region including the provinces of Alberta and British Columbia, and +29 µg m$^{-3}$ for the sub-region comprising the states of
490 Idaho, Montana, Oregon and Washington, respectively). At least part of the positive biases may be due to 10km GEM-MACH
491 forest fire emissions occurring in the state of Alaska being overestimated during the study period. However, the ECMWF
492 reanalysis also captures significant particulate mass crossing the Bering Strait from fires in Siberia during this period, so the
493 relative contributions of fires within the low resolution GEM-MACH domain and the ECMWF boundary conditions driving
494 that domain are combined, and can't be separated in the runs carried out here.

495  The local AOD positive biases associated with fires could also be the result of the mixing state assumptions of the Mie code

496  used here for generating aerosol optical properties. These assumptions may also account for negative AOD biases over much

497  of the remainder of the model domain. As noted earlier, this overall negative bias of AOD predictions (both boundary condition

498  configurations result in observation:model slopes less than unity) is a common problem in air-quality models, and may be due

499  to assumptions regarding the model mixing state (Curci *et al.,* 2015). That comparison of multiple mixing state assumptions

500  on AOD with observations for European and North American modelling domains (Curci *et al.,* 2015), showed a typical factor

501  of two model under-prediction of 440 nm North American AOD across all mixing state assumptions, with European AOD

502  negative biases ranging from unbiased to a factor of 2. These earlier findings along with overestimates at forest fire plumes

503  with our current homogeneous mixture approach at 550nm suggest that the hygroscopic growth may be overestimated for

504  forest fire particles, in turn overestimating forest fire AODs locally, while external mixing assumptions may be required to

505  improve model AOD performance elsewhere in the model domain.

506  We note that the combined use of the ECMWF global reanalysis and a 10km resolution GEM-MACH simulation to provide

507  boundary conditions for our 2.5km domain resulted in a degradation of model performance for surface PM2.5, $O_3$, and $NO_2$,

508  for 71 out of 96 statistical scores, compared to the use of a MOZART2009 reanalysis for 2.5km domain boundary conditions.

509  The improvement associated with the use of feedbacks was maintained, showing that the impact of feedbacks is a robust

510  finding. However, the performance degradation associated with the change of boundary conditions is a source of concern.

511  We also note that, while AOD performance has improved with the use of the ECMWF + GEM-MACH10km boundary

512  conditions in Figure 14, significant overestimates of AOD occur with the use of these boundary conditions, in several regions

513  in the USA. This may be seen by comparing Figure 14 (a) and Figure 14 (b) for the states of Montana, Wyoming, Nevada,

514  New Mexico and Utah, where the dark blue colours in the observations (14(a)) indicate observed AODs less than 0.01, whereas

515  the ECMWF+GEM-MACH 10km driven simulation (14(b)) indicate values of 0.03 to 0.05). This is consistent with the

516  increase in positive surface bias in PM2.5 associated with the use of the ECMWF + GEM-MACH 10km boundary conditions

517  (e.g., Feedback runs having Western Canada and Western USA positive biases of PM2.5 of 4.578 and 1.805 $\mu g\ m^{-3}$ (Table 1),

518  compared to the MOZART2009 reanalysis driven run values of 0.236 and -1.786 $\mu g\ m^{-3}$, Table A2, respectively). The

519  boundary condition setup thus accounts for a substantial increase in overall surface PM2.5 mass, with the use of

520  ECMWF+GEM-MACH 10km increasing mean PM2.5 by 4.34 and 3.59 $\mu g\ m^{-3}$ in western Canada and USA respectively

521  relative to the use of MOZART2009.

522  The reduction in performance may thus be due to two possible causes (or their combination): (1) the domain within the GEM-

523  MACH 10km simulation might be sufficiently large, and the emissions in the regions between the 10km boundaries and the

524  2.5km domain sufficiently in error, that the 2.5km simulation accuracy is adversely affected; (2) the ECMWF reanalysis

525  employed on the outermost boundary of the 10km domain contributes sufficient PM2.5, $NO_2$ and $O_3$ to the simulations that

526  the innermost domain model performance at the surface is adversely affected. That is, the degradation in performance may be

527  associated with the GEM-MACH 10km simulation, the ECMWF reanalysis, or a combination of both factors.

In order to examine the potential impact of the ECMWF reanalysis used as the outermost domain boundary conditions, we evaluated the ECMWF reanalysis using the same observation data, station locations, and performance metrics as was used for our 2.5km simulations – the results of this analysis are shown in Supplemental Information Tables A3 (PM2.5), A4 ($O_3$) and A5 ($NO_2$). This additional analysis shows that the ECMWF reanalysis values during the study period have higher positive biases for PM2.5 and $O_3$, and lower negative biases for $NO_2$, than the corresponding 2.5km GEM-MACH simulations. A similar pattern occurs for the other statistical metrics, with the ECMWF reanalysis usually having a reduced performance for most statistical scores for PM2.5, $O_3$, and $NO_2$ over the study region in comparison to the high resolution model simulations carried out here. The ECMWF reanalysis was also evaluated for the same time period for the entire North American domain, in Tables A3 to A5; the scores for this last analysis suggest that the performance of the reanalysis relative to observations is similar over the continent, and is not limited to our study area. We note that the ECMWF reanalysis has relatively low spatial and time resolution compared to the 2.5km simulations carried out here ($0.75^{o}$x$0.75^{o}$ versus 2.5 km x 2.5km, 3 hourly output values compared to 1 hour output values), and relatively coarse resolution for particle sizes (e.g. 3 size bins compared to the 12 bins used within GEM-MACH; these issues may factor into the performance scores. The comparison does not rule out the possibility that GEM-MACH's 10km resolution simulations may *also* contribute adversely to our 2.5km model performance. However, our analysis suggests that our use of the ECMWF reanalysis for boundary conditions on our outermost domain likely accounts for at least some of the performance degradation in our modelling system, compared to the MOZART2009 boundary condition simulation carried out earlier.

**3.3 Model Evaluation Summary**

Overall, the incorporation of feedbacks in this study has resulted in improvements in weather and air-quality forecast accuracy, *albeit with some caveats*. Weather forecast variables showed improvements at the 90% confidence level for several fields, and vertical profiles showed a matching performance or improvements at most levels and times. Total precipitation scores also showed minor improvements or matching performance at the 90% confidence level. A previously unexpected spin-up issue specific to on-line coupled models was noted: the impact of on-line coupled particulate matter on cloud variables was sufficiently strong that cloud field adjustment in the first 6 hours of the forecast was required prior to some weather forecast variable improvements to be apparent (surface pressure, dewpoint temperature, sea-level pressure). While the current forecast cycling duration was constrained by operational requirements, this suggests that forecast cycling should include both air-quality and meteorological variables during on-line coupled forecast spin-up periods. That is, the model tracer concentrations 6 hours prior to the current forecast start-up could also be used during the initial meteorological spin-up period, thus allowing chemistry and cloud formation to spin-up simultaneously. Scores for surface PM2.5, $NO_2$, and $O_3$ also generally improved with the incorporation of feedbacks (35 out of 48 comparisons showed improvements). The choice of lateral boundary conditions was shown to have a significant impact on chemical performance within the model domain. In comparison to satellite-based AOD values, the current model's AOD values were generally biased low, with smaller magnitude biases being associated with the ECMWF + 10-km GEM-MACH boundary conditions. The latter comparison also showed that large fires

17

561     off-domain in Alaska and Siberia likely had a large impact on AODs in the eastern and northern section of the model domain,

562     through comparison with our initial simulations.

563

564     **4 Effects of Feedbacks on Selected Simulation-Period Average Variables**

565     In this section, we compare time averages of the entire study period for the two simulations, both at the surface and in vertical

566     cross-sections through the model domain, to illustrate some of the changes in both weather and air-quality associated with the

567     incorporation of feedbacks. We have found differences at greater than 90% confidence between the predicted meteorological

568     and chemical forecasts in the vicinity of the Alberta/Saskatchewan forest fires, as well as in contrasting changes between land

569     and sea. We note again here that the "no-feedback" simulation makes use of time and spatially invariant aerosol CCN and

570     optical properties, within the meteorological portion of the model. The comparisons thus show the differences associated with

571     the use of climatological constant aerosol properties, and the on-line coupled model-generated aerosols.

572     As in the meteorological evaluation, we have made use of 90% confidence levels in order to gauge the level of significance of

573     the differences between the feedback and no-feedback simulations in the following analysis.

574     The approach for representing model grid value 90% confidence levels is described in detail in SI Appendix A2. The

575     differences in the mean grid cell values between the simulations for which the above quantity is greater than unity differ at or

576     greater than the 90% confidence level. Differences in the mean values, as well as the value of the above ratio, are thus reported

577     in the following section.

578     **4.1 Effects of Feedbacks on Time-Averaged Meteorology**

579     The feedback – no-feedback differences in the simulation-period average cloud droplet number density (number kg$^{-1}$ of air)

580     and mass density (g water kg$^{-1}$ of air) along centred cross-sections spanning the length and width of the 2.5-km resolution

581     model domain are shown in Figure 15 (cross-section locations are shown in Figure 1). The "Ocean", "Land", and "Forest

582     Fire" regions identified are with reference to the approximate locations of these features along these cross-sections. Figure 15

583     also shows the confidence ratio values as described above – regions where the predicted mean values differ at or above the

584     90% confidence level are shown in red, while those differences below the 90% confidence interval are shown in blue.

585     Feedbacks increase the cloud droplet number density over the northern part of the domain, including the region impacted by

586     the Alberta/Saskatchewan forest fires, from the surface up to about 500 mb (roughly equivalent to hybrid level 0.500), and

587     decrease at higher elevations further to the south and along the length of the model domain into the western USA (Figure

588     15(a)). Cloud droplet numbers also decrease over the ocean, but increase eastwards over the land (Figure 15(b)). The latter is

589     unrelated to the forest fires; this is an indication that the modelled aerosol number concentration over the ocean is much lower

590     than the single climatological aerosol population assumed in the no-feedback run, resulting in lower cloud droplet number

591     concentrations. The changes are significant at the 90% confidence level from the surface up to hybrid level 0.60 in the northern

592     region which is most impacted by forest fire smoke, and in isolated regions further aloft along the south to north cross-section

593     (Figure 15(c)), and over the regions of the ocean in the west to east cross-section (Figure 15(d)). Higher-than-climatology

18

594 aerosol loadings, a large portion of which are due to the forest fires, resulted increased cloud droplet number densities in the

595 lower troposphere, while decreasing them in the mid-to-upper troposphere (Figure 15(a)). This impact of feedbacks is in

596 accord with the satellite observations of Saponaro *et al.* (2017), and was also seen in Takeishi *et al.* (2020). In contrast, cloud

597 droplet mass density (i.e. cloud liquid water content) largely decreases across the domain along the north-south cross-section

598 (Figure 15(e)), as well as over the ocean, with a varying pattern over the land in the east-west cross-section (Figure 15(f)). The

599 magnitudes and significance levels for the average change in cloud droplet mass are lower than for cloud droplet number, with

600 the most significant differences occurring over the ocean (Figure 15(g,h)).

601 Consistent with the cloud droplet number changes, rain droplet numbers and mass mixing ratios increase aloft with the

602 feedback simulation, over both the forest region impacted by the forest fires (Figure 16(a,e)) and over the ocean (Figure

603 16(b,f)), with a varying impact over the land and more distant from the forest fire sources (Figure 16(f)). The changes are

604 significant at the 90% confidence level for rain droplet number in these regions (compare Figure 16(a) with 16(c); 16(b) with

605 16(d)), while the rain droplet mass changes sometimes reach but are usually below the 90% confidence level (Figure 16(g,h)).

606 These results suggest that relative to the no-feedback simulation, which employs climatological aerosol CCN properties, the

607 AIE in the feedback simulation is causing significant change in hydrometeor numbers, and a less significant increase in

608 hydrometeor mass. In the forest fire-impacted region, the ADE and AIE in the feedback simulation significantly increase the

609 number of cloud droplets near the surface and throughout the middle to upper troposphere (Figure 15(a,c)). The rain drop

610 number in the middle troposphere (Figure 16(a,c)) also increases significantly between hybrid levels 0.90 to 0.70 (Figure

611 16(e,g)). Near-surface rain drop number and rain drop mass differences throughout the cross sections (Figure 16(e,f)) fall

612 below the 90% confidence level (Figure 16(g,h).

613 Over the oceans, water droplet number and mass both decrease (Figure 15(b,f)), and raindrop number and mass increase

614 (Figure 16(b,f)); more atmospheric water is converted to rain drops as a result of the feedbacks, relative to the climatology in

615 the no-feedback simulation. However, these changes are more significant aloft than at the surface, with the difference in both

616 rain drop number and mass falling below the 90% confidence level near the surface. We interpret these changes as a shift in

617 over-ocean liquid hydrometeor numbers and to a lesser degree the water mass aloft from cloud droplets to rain drops due to

618 the AIE in the feedback setup relative to the climatology of the no-feedback simulation. The changes occur at the 90%

619 confidence level aloft, but the near-surface changes are smaller and are usually below the 90% confidence level.

620 Differences in the average surface precipitation flux and the confidence ratio values are shown in Figure 17. Changes in

621 average precipitation (Figure 17(a)) appear random, though locally these differences are significant at the 90% confidence

622 level (Figure 17(b)). Both the magnitude of the differences and the frequency in their reaching the 90% confidence level

623 increase south-westwards. Given the local and episodic nature of rainfall events, the high level of significance in this case

624 probably results from the presence or absence of individual rainfall events between the two simulations affecting the local

625 average and standard deviations.

626 Several systematic changes in the average values of the model's meteorological output fields were noted due to the use of

627 feedbacks relative to aerosol property climatologies (Figure 18), although all fall below the 90% confidence level for the

19

difference in the mean values between the two simulations (Figure 19). Specific humidity increased in the region most affected by fires (Figure 18(a), surface air temperature decreased below the smoke plumes while increasing further south (Figure 18(b)), while dewpoint temperature decreased (Figure 18(c)), implying a decrease in relative humidity with feedbacks. Surface pressure increased over the land (mostly east of the Rockies), particularly in the region downwind of the Alberta / Saskatchewan fires while decreasing over the ocean (Figure 18(d)). Planetary boundary layer height increased over the land (Figure 18(e)) except in the immediate vicinity of the Alberta/Saskatchewan fires, consistent with decreased atmospheric stability in the lowest part of the atmosphere. The friction velocity also increased with the use of feedbacks (Figure 18(f)); this is consistent with a decrease in stability and an increase in turbulent energy   The air temperature increases occur at the surface south of the forest-fire impacted region and above roughly 750 mb, decreasing temperatures from the surface in the forest-fire impacted region up to 750 mb (Figure 20 (a,b)). Feedbacks thus increase near-surface temperatures, relative to the no-feedback meteorological model's simple aerosol climatology, in regions far from the fires, decreasing them near the fires, decrease temperatures in the lower free Troposphere, and increase temperatures further aloft. All of these differences between feedback and no-feedback simulations, despite their large geographic range, fall below the local 90% confidence ratio. However, when the differences in air temperature resulting associated with feedback and no-feedback forecasts are compared to observations across the entire domain (as opposed to at gridpoint locations as in Figures 18 and 19) the 90% confidence level is exceeded both at the surface at specific forecast times (Figure 6(a)), and at multiple heights aloft at the 12th and 24th forecast hours (Figures 12, 13).

**4.2 Effects of Feedbacks on Time-Averaged Chemistry**

In the previous meteorological impacts section, changes in aerosol loading relative to the climatology, dominated by forest fires, were shown to have a significant impact on cloud formation and atmospheric temperatures through ADE and AIE. These might be expected to in turn influence and be influenced by particulate matter emitted by the forest fires, with the plume rise of the forest fires dependent on the meteorological changes. Air temperatures increase slightly in the model surface layer south of the fires (Figure 18(b), +0.01 to +0.05 $^{\circ}$C) but decrease at greater magnitudes through the rest of the lower Troposphere (surface near the fires to hybrid level 0.749, Figure 20(a)), with a maximum decrease of -0.5$^{\circ}$C between hybrid levels 0.893 and 0.848. The reduction in temperatures between hybrid levels 0.90 to 0.70 from the impact of the smoke plumes is similar to the findings of Saponaro *et al.* (2017). These changes air temperatures implies a decrease in near-surface atmospheric stability associated with feedbacks, given that the overall temperature gradient from the surface has become more negative (that is, the ambient lapse rate has increased). Rising air parcels will follow an adiabatic lapse rate; these increases in the ambient lapse rate imply that rising air parcels will have an increasing tendency to be warmer than their environment. Feedbacks have thus reduced atmospheric stability within the forest fire smoke in the lowest part of the atmosphere; the atmosphere there has become more unstable. Meanwhile, the feedbacks decrease the environmental lapse rate further aloft above the forest fire smoke, between hybrid levels 0.848 and 0.339. Rising air parcels in this region following an adiabatic lapse rate will thus have an increasing tendency to be colder than their environment – the atmosphere above the smoke plumes

661 has become more stable. This is echoed by the response of the concentration fields to the near-surface stability change, as can
662 be seen through comparisons of the PM2.5, $NO_2$ and $O_3$ surface concentrations changes (Figure 21) and as vertical cross-
663 sections (Figures 22, 23, 24), respectively.

664 Changes above the 90% confidence level for PM2.5 and $NO_2$ occur near the forest fires themselves (red regions, near top of
665 model domain, Figure 21(a,b)), though remain below 90% confidence for O3 (Figure 21(c)).

666 Feedbacks result in near-surface PM2.5 decreases in the regions downwind of the forest fires (Figure 21(a), Figure 22(a), note
667 the large blue region and more intense blue region near surface in Figure 22(a)), suggesting less PM2.5 mass is present near
668 the surface due to the feedbacks. Given the increase in near-surface stability below the fire plumes noted above, this change
669 in the vertical distribution probably reflects a decrease in downward diffusive mixing of the forest fire plumes once aloft – the
670 feedbacks thus have a tendency to increase the smoke plume concentrations aloft, by preventing the downward mixing of
671 smoke injected by the fires. These PM2.5 concentration effects rise above the 90% confidence level within the region closest
672 to the fires.

673 Feedbacks result in an increase in near-surface $NO_2$ in several inland urban centers and less $NO_2$ at surface level downwind
674 (Figure 21(b), though these differences are only significant at the 90% confidence level within the forest fire plumes (Figure
675 21(e), Figure 23(c)). Ocean versus land $NO_2$ differences remain below the 90% confidence level.

676 Feedbacks decreased lower Troposphere $O_3$ near the forest fires (Figure 21(c), Figure 24(a)), while increasing $O_3$ near above
677 hybrid level 0.383. The forest fires are also the only area where the differences in between mean ozone forecasts approach
678 90% confidence.

679 Overall, the most significant effects of the feedbacks were: (1) increases in PM2.5 aloft and decreases near the surface in areas
680 impacted by the fires, and (2) increases in $NO_2$ aloft and decreases near the surface near the fires, to lesser extent than PM2.5,
681 and (3) decreases in lower troposphere $O_3$, particularly near the surface in the region impacted by the fires.

682 The feedback-induced changes in primary and secondary pollutants in the forest fire regions are consistent with the decrease
683 in atmospheric stability noted above – a greater proportion of the primary particulate matter and $NO_2$ resulting from near-
684 surface forest fire emissions of NO remain aloft with the addition of feedbacks. The decrease in surface ozone and increase
685 further aloft in the fire region (Figure 24(a)) spatially matches the decrease in surface $NO_2$ (Figure 22(a)). Chemically, this
686 may imply that the changes associated with feedbacks occur in NOx-limited environments, i.e., with relatively high VOC/NOx
687 ratios, since in these environments, decreases in NOx emissions may lead to decreases in the rate of secondary $O_3$ formation.
688 Alternatively, the reduction in near-surface $O_3$ concentrations may reflect a decrease in light levels reaching the surface due to
689 cloud attenuation (aerosol indirect effect), with the resulting lower photolysis rates resulting in a reduction in surface
690 photochemical ozone production.

691 Our analysis thus suggests a net enhanced upward transport occurs in forest fire plumes due to feedbacks, and that this transport
692 is linked to feedback-induced:
693      (1) Increases in local near-surface atmospheric stability, reducing downward mixing of particulate plumes once aloft
694 (Figure 22(a));

21

695         (2) Increases in cloud droplet numbers throughout the lower troposphere (Figure 15(a)); and

696         (3) Increases in rain drop numbers aloft (Figure 16(a)).

697         This combination suggests the presence of an AIE feedback loop – increased lower atmosphere stability results a
698 greater proportion of particulate matter remaining aloft, in turn resulting in more particles remaining at higher levels in the
699 atmosphere where they may act as cloud condensation nuclei, increasing cloud droplets aloft (Figure 15(a)). This in turn
700 results in increased lower middle troposphere cooling, through the 1$^{st}$ AIE (increase in cloud droplet numbers aloft leading to
701 increased cloud albedo and cooling of the atmosphere below the cloud tops) while the corresponding decreases in particles and
702 cloud condensation nuclei at lower levels results in a smaller near-surface impact on the AIE and ADE, hence relatively minor
703 changes on near-surface temperatures (Figure 20(a)). This combination maintains a feedback-induced near-surface unstable
704 temperature gradient, relative to the no-feedback simulation employing aerosol property climatologies. We acknowledge that
705 these changes in temperature fall below the 90% confidence level for the averages over all times, though note that differences
706 in mean bias relative to observations for the two simulations became significantly different at specific times of day in the
707 forecasts (Figure 6(a), hours 3, 6, 15 and 18, corresponding to 15, 18, 3 and 6 UT, or 9 AM, 12 noon, 9 PM, and midnight
708 MDT), implying that the temperature changes at these specific times reach a higher level of significance. Similarly, Figures
709 12 and 13 show reductions in the near-surface temperature biases with the use of feedbacks.

710 **4.3 Summary, Differences in Forecast Simulation-Period Averages**

711 Relative to the no-feedback simulation employing an aerosol climatology, the AIE feedback as simulated here is associated
712 with increases in near-surface stability over both ocean and forest-fire influenced land areas. Over oceans, near-surface
713 particulate matter is removed as cloud condensation nuclei, resulting in increased cloud droplet numbers, maintaining the
714 temperature gradient through the 1$^{st}$ aerosol indirect effect. In the vicinity of forest fires, increases in near-surface stability
715 result in more PM2.5 remaining aloft, increasing the availability of cloud condensation nuclei aloft, increasing cloud droplet
716 numbers aloft, hence also maintaining the less stable near-surface temperature gradient through the 1$^{st}$ aerosol indirect effect.
717 We note that the ADE may also play a weak role, particularly in the southern part of the domain, where lower atmosphere
718 temperature gradient increases are not accompanied by significant changes in cloud droplet numbers (Figure 15(a), southern
719 half of the cross-section), but are accompanied by significant though small magnitude increases in PM2.5 in the lower
720 atmosphere (Figure 22(a), southern half of cross-section), and temperature profile changes (Figure 20) below the 90%
721 confidence level.

722

723 **5 Conclusions**

724 The work carried out here suggests that the answers to our two research questions ("Can on-line coupled models improve both
725 air-quality and meteorological forecasts?" and "Are the changes in forest fire forecasts associated with implementing forest
726 fire emissions within a on-line coupled model sufficient to significantly perturb weather and chemistry?") are both a *qualified*
727 "yes". Within the high resolution domain size employed here, improvements or matching weather forecast performance was

728 seen for most times and heights in the atmosphere, at greater than 90% confidence. Improvements in model performance for

729 surface PM2.5, $NO_2$ and $O_3$ were also found, across most statistical measures (35 out of 48 statistical evaluation scores showed

730 improvements). Comparing average vertical cross-sections, the chemical concentration changes associated with feedbacks

731 were the most significant close to the forest fires in the northern portion of the domain. There, increased net vertical transport

732 associated with decreased near-surface stability lowered near-surface PM2.5 and $NO_2$ concentrations and increased them aloft,

733 and resulted in reduced surface $O_3$.

734 Our simulations suggest that aerosol optical depth in the region, as well as the overall chemical performance of the model, was

735 strongly influenced by upwind boundary conditions. AODs were biased low despite PM2.5 positive biases, suggesting that

736 the homogeneous mixture approach for aerosol optical properties results in a general under-prediction of aerosol optical depths,

737 in accord with Curci *et al.* (2015), and that obtaining better data for forest fire aerosol optical properties should be a priority

738 for future study, as well as an examination of external mixture approaches. Positive AOD biases in the region affected by fires

739 suggests that forest fire plumes have significantly different optical properties, and may be less hygroscopic, than industrial

740 aerosols of comparable size. Special / separate treatment of forest fire CCN and optical properties are therefore also

741 recommended in future work.

742 On-line coupling forest fire plume rise calculations with the weather parameters was shown to have a significant impact on the

743 height of primary pollutants reached by forest fires, the formation of near-surface ozone near the forest fires, and on particulate

744 matter. These changes were largely driven by the AIE, which maintains an increased lapse rate (decreased near-surface

745 stability) over the forest-fire-influenced and oceanic portions of the region studied. Weak evidence for the influence of the

746 ADE was shown in the southern part of the domain, where increases in particulate matter were also accompanied by decreases

747 in stability between the surface and the lower-middle troposphere (the differences were at a lower than 90% confidence level

748 for these comparisons of temperatures averaged over all model times).

749 Relative to the no-feedback aerosol climatology for CCN and aerosol optical properties, the simulations carried out here

750 suggested that in the vicinity of forest fires feedbacks significantly increase cloud droplet number densities near the surface

751 and aloft, and significantly increase rain drop number densities aloft, relative to forecasts driven by climatological aerosol

752 properties. Over the oceans, feedbacks decreased cloud droplet number density and increased rain drop number density aloft,

753 relative to the simulation employing invariant CCN properties. Oceanic cloud droplet mass increased to a lesser degree (with

754 smaller regions above the 90% confidence level), as did rain drop mass (the mean differences for which for the most part

755 remained below the 90% confidence level). This provides some evidence for a shift in atmospheric water mass associated

756 with feedbacks from cloud water to rain over the oceans relative to the no-feedback climatology, though this shift occurred

757 largely within the variability of the cloud fields within each simulation. Longer simulations may be needed to achieve higher

758 confidence in this finding.

759

760 **Data Availability**

The datasets used here for model evaluation are available from the publicly accessible websites (AQS network) https://www.epa.gov/aqs and (NAPS network) http://maps-cartes.ec.gc.ca/rnspa-naps/data.aspx.

## Author Contribution

PAM: experiment design, conceptualization, analysis, writing of manuscript drafts; AA: model code and run script design and implementation, statistical analysis of model results, model analysis graphics; JC: forest fire emissions processing system design and coding, manuscript contributions, draft review and assistance; BP: forecast system simulations and design; WG: indirect effect updates, advice on P3 implementation, manuscript contributions, manuscript review; CS: code version contributions, manuscript review; CS: AOD analysis, manuscript contributions and review; KS: forest fire emissions processing system design and coding, manuscript contributions and review; PC: forecast system simulations and design; JZ: emissions processing and input field assistance, manuscript review and contributions; J.M.: indirect effect updates and advice on implementing AIE in the P3 scheme, manuscript review and contributions.

## Competing Interests

The authors declare that they have no conflict of interest.

## References

Abdul-Razzak, H., and Ghan, S.J.: A parameterization of aerosol activation. 3. Sectional representation, J. Geophys. Res Atm., 107 (D3), http://dx.doi.org/10.1029/2001JS000483, 6 pp, 2002.

Aggarwal, R., and Ranganathan, P., Common pitfalls in statistical analysis: the use of correlation techniques, Perspect. Clin. Res., 187-190, 2016.

Ahmadov, R., James, E., Grell, G., Alexander, C., Benjamin. S., McKeen, S., Pereira, G., Freitas,S., Csiszar, I., Tsidulko, M., Kondragunta, S., Xu, C., Wong, K.Y., and Albers, S.: Forecasting smoke, visibility and smoke-weather interactions using a coupled meteorology-chemistry modeling system: Rapid Refresh and High-Resolution Rapid Refresh coupled with Smoke (RAP/HRRR-Smoke) , EGU 2019 Conference presentation, Geophysical Research Abstracts, Vol. 21, EGU2019-18605, 2019. https://meetingorganizer.copernicus.org/EGU2019/EGU2019-18605.pdf, 2019.

Akingunola, A., Makar, P.A., Zhang, J., Darlington, A., Li, S.-M., Gordon, M., Moran, M.D., and Zheng, Q.: A chemical transport model study of plume-rise and particle size distribution for the Athabasca oil sands, Atm. Chem. Phys., 18, 8667-8688, 2018.

Albrecht, B.A.: Aerosols, cloud microphysics, and fractional cloudiness, Science, 245(4923), 1227-1230, https://doi.org/10.1126/science.245.4923.1227, 1989.

791    Baro, R., Palacios-Pena, L., Baklanov, A., Balzarini, A., Brunner, D., Forkel, R., Hirtl, M., Honzak, L., Perez, J.L., Pirovano,
792        G., San Jose, R., Schroder, W., Werhahn, J., Wolke, R., Zabhar, R., Jimenez-Guerrero, P.: Regional effects of
793        atmospheric models on temperature: an evaluation of an ensemble of online coupled models, Atm. Chem., Phys., 17,
794        9677-9696, 2017.

795    Briggs, G.A.: A plume rise model compared with observations, J. Air. Poll. Cont. Assoc., 15, 433-438,
796        https://doi.org/10.1080/000022470.1965.10468404, 1965.

797    Briggs, G.A.: Plume rise and buoyancy effects, atmospheric sciences and power production, in: DOE/TIC-
798        27601(DE84005177), edited by Randerson, D., Technical Information Center, U.S. Dept. of Energy, Oak Ridge, TN,
799        USA, 327-366, 1984.

800    Carrera, M.L., Belair, S., Bilodeau, B.: The Canadian Land Data Assimilation System(CalDAS): description and synthetic
801        evaluation study, J. Hydrometeor., 16, 1293-1314, 2015.

802    Carslaw, D.C., and Ropkins, K., openair – An R package for air quality data analysis, Env. Mod. Soft., vol. 27-28, pp 52-61,
803        2012.

804    Chen, J., Anderson, K., Pavlovic, R., Moran, M.D., Englefield, P., Thompson, D.K., Munoz-Alpizar, R., and Landry, H.: The
805        FireWork v2.0 air quality forecast system with biomass burning emissions from the Canadian Forest Fire Emissions
806        Prediction System v2.03, Geosci. Model Dev., 12, 3283–3310, 2019.

807    Clark, T.L., Coen, J. and Latham, D.: Description of a coupled atmosphere–fire model. International Journal of Wildland
808        Fire, 13(1), pp.49-63, 2004.

809    Clark, T.L., Jenkins, M.A., Coen, J.L., Packham, D.R.: A coupled atmosphere-fire model: role of convective froude number
810        and dynamic engineering at the fireline, Int. J. Wildland Fire, 6, 177-190, 1996.

811    Coen, J. Cameron, M., Michalakes, J., Patton, E., Riggan, P., and Yedinak, K., WRF-Fire: coupled weather-wildfire
812        modelling with the Weather Research and Forecasting Model, J. Appl. Meteorol. Climatol., 52, 16-38, 2013.

813    Côté, J., Gravel, S., Méthot, A., Patoine, A., Roch, M., Staniforth, A.: The operational CMC/MRB global environmental
814        multiscale (GEM) model. Part 1: design considerations and formulation. Mon. Wea. Rev., 126, 1373-1395, 1998.

815    Curci, G., Hogrefe, C., Bianconi, R., Im, U., Balzarini, A., Baro, R., Brunner, D., Forkel, R., Giordano, L., Hirtl, M., Honzak,
816        L., Jimenez-Guerrero, P., Knote, C., Langer, M., Makar, P.A., Pirovano, G., Perez, J.L., San Jose, R., Syrakov, D.,
817        Tuccella, P., Werhahn, J., Wolke, R., Zabkar, R., Zhang, J., and Galmarini, S.: Uncertainties of simulated aerosol optical
818        properties induced by assumptions on aerosol physical and chemical properties: an AQMEII2 perspective, Atm. Env.,
819        115, 541-522, 2015.

820    Duveiller, G., Fasbender, D, and Meroni, M., Revisiting the concept of a symmetric index of agreement for continuous
821        datasets, Sci. Rep., 6, 19401; doi:10.1038/srep19401, 2016.

822    Ezhova, E., Ylivinkka, I., Kuusk, J., Komsaare, K., Vana, M., Krasnova, A., Noe, S., Archinov, M., Belan, B., Park, S-B.,
823        Lavric, J.V., Heimann, M., Petaja, T., Vesala, T., Mammarella, I., Kolari, P., Back, J., Rannik, U., Kerminen, V.-M., and

824      Kulmala, M.: Direct effect of aerosols on solar radiation and gross primary production in boreal and hemiboreal forests,

825      Atm. Chem. Phys., 18, 17863-17881, 2018.

826 Fox, D.G., Judging air quality model performance – a summary of the AMS workshop on dispersion model performance,

827      Bull. Am. Met. Soc., 62, 599-609, 1981.

828 Galmarini, S., Hogrefe, C., Brunner, D., Makar, P., Baklanov, A., Preface, Atm. Env., 115, 340-344, 2015.

829 Geer, A.J.: Significance of changes in medium-range forecast scores, Tellus A., 68, 30229,

830      http://dx.doi.org/10.3402/tellusa.v68.30229, 2016.

831 Girard, C., Plante, A., Desgagne, M., McTaggart-Cowan, R., Cote, J., Charron, M., Gravel, S., Lee, V., Patoine, A., Qaddouri,

832      A., Roch, M., Spacek, L., Tanguay, M., Vaillancourt, P.A., and Zadra, A.: Staggered vertical discretization of the

833      Canadian Environmental Multiscale (GEM) model using a coordinate of the log-hydrostatic-pressure type. *Mon. Wea.*

834      *Rev.*, 142, 1183–1196, 2014.

835 Gong, S.L. Barrie, L.A., Blanchet, J.-P., von Salzen, K., Lohmann, U., Lesins, G., Spacek, L., Zhang, L.M., Girard, E., Lin,

836      H., Leaitch, R., Leighton, H., Chylek, P., Huang, P." Canadian Aerosol Module: a size-segregated simulation of

837      atmospheric aerosol processes for climate and air quality models. 1. Module development. J. Geophys. Res., 108, 4007,

838      http://dx.doi.org/10.1029/201JG002002, 2003.

839 Gong, W., Beagley, S.R., Zhang, J., Cousineau, S., Chen, J., Sassi, M., Munoz-Alpizar, R., Morrison, H., Lyons, L., and

840      Bellavance, P.: Modelling regional air quality in the Canadian Arctic: impact of North American wildfire and Arctic

841      shipping emissions, in: Air Pollution Modelling and Its Application, XXIV, edited by Steyn, D.G. and Chaumerliac, N.,

842      Springer, Switzerland, 301-306, 2016.

843 Gong, W., Makar, P.A., Zhang, J., Milbrandt, J, Gravel, S., Hayden, K.L., Macdonald, A.M., Leaitch, W.R.: Modelling

844      aerosol-cloud-meteorology interaction: a case study with a fully coupled air quality model (GEM-MACH), Atm. Env.,

845      115, 695-715, 2015.

846 Grell, G.A., and Freitas, S.R., A scale and aerosol aware stochastic convective parameterization for weather and air quality

847      modelling, Atmos. Chem. Phys., 14, 5233-5250, 2014.

848 Griffin, D., Sioris, C., Chen, J., Dickson, N., Kovachik, A., De Graaf, M., Nanda, S., Veefkind, P., Dammers, E., McLinden,

849      C.A. and Makar, P., The 2018 fire season in North America as seen by TROPOMI: aerosol layer height intercomparisons

850      and evaluation of model-derived plume heights. Atmospheric Measurement Techniques, 13(3): 1427-1427, 2020.

851 Hanna, S.R., Air quality model evaluation and uncertainty, J. Air Poll. Control Assoc., 38, 406-412, 1988.

852 Hoegh-Guldberg, O., Jacob, D., Taylor, M., Bindi, Brown, S., Camilloni, I., Diedhiou, A., Djalante, R., Ebi, K.L.,

853      Engelbrecht, F., Guiot, J., Hijioka, Y., Mehrotra, S., Payne, A., Seneviratne, S.I., Thomas, A., Warren, R., and Zhou,

854      G.: Impacts of 1.5ºC Global Warming on Natural and Human Systems. In: *Global Warming of 1.5°C. An IPCC Special*

855      *Report on the impacts of global warming of 1.5°C above pre-industrial levels and related global greenhouse gas*

856      *emission pathways, in the context of strengthening the global response to the threat of climate change, sustainable*

857      *development, and efforts to eradicate poverty* [Masson-Delmotte, V., Zhai, P., Pörtner, H.-O., Roberts, D., Skea, J.,

858    Shukla, P.R., Pirani, A., Moufouma-Okia, W., Péan, C., Pidcock, R., Connors, S., Matthews, J.B.R., Chen, Y., Zhou,
859        X., Gomis, M.I., Lonnoy, E., Maycock, T., Tignor, M., and Waterfield, T. (eds.)]. In Press, 2018.

860    Inness, A., Ades, M., Agusti-Panareda, A., Barre, J., Benedictow, A., Blechschmidt, A.-M., Dominguez, J.J., Engelen, R.,
861        Eskes, H., Flemming, J., Huijnen, V., Jones, L., Kipling, Z., Massart, S., Parrington, M., Peuch, V-H., Razinger, M.,
862        Remy, S., Schulz, M., and Suttie, M., The CAMS reanalysis of atmospheric composition, Atmos. Chem. Phys., 19, 3515-
863        3556, 2019.

864    James, E., Ahmadov, R., and Grell, G.: Realtime Wildfire Smoke Prediction in the United States: the HRRR-Smoke Model,
865        in: EGU General Assembly Conference Abstracts, vol. 20 of EGU General Assembly Conference Abstracts, p. 19526,
866        2018

867    Jiang, Y., Yang, X-Q., and Liu, X., Seasonality in anthropogenic aerosol effects on East Asian climate simulated with CAM5,
868        J. Geophys. Res. Atmos., 120, 10837-10861, doi:10.1002/2015JD023451, 2015.

869    Jouan, C., J.A. Milbrandt, P. Vaillancourt, F. Chosson, H. Morrison: Adaptation of the Predicted Particles Properties (P3)
870        microphysics scheme for large-scale numerical weather prediction. *Wea. Forecasting* (under review), 2020.

871    Jung, J., Souri, A.H., Wong, D., Lee, S., Jeon, W., Kim, J., Choi, Y.: The impact of the direct effect of aerosols on meteorology
872        and air quality using aerosol optical depth simulation during the KORUS-AQ campaign, J. Geophys. Res. Atm., 124,
873        8303-8319, https://doi.org/10.1029/2019JD030641, 2019.

874    Kochanski, A.K., Jenkins, M.A., Yedinak, K., Mandel, J., Beezley, J., and Lamb, B., Toward an integrated system for fire,
875        smoke and air-quality simulations. Int. J. Wildland Fire, 25, 534-568, 2016.

876    Kochanski, A.K., Malia, D.V., Fearon, M.G., Mandel, J., Souri, A.H., and Brown, T., Modelling wildfire smoke feedback
877        mechanisms using a coupled fire-atmosphere model with a radiatively active aerosol scheme, J. Geophys. Res. Atm,
878        124, 9099-9116, 2019.

879    Krause, P, Boyle, D.P., Base, F., Comparison of different efficiency criteria for hydrological model assessment, Adv.,
880        Geosci., 5, 89-97, 2005.

881    Legates, D.R., and McCabe, G.J. Jr, Evaluating the use of "goodness-of-fit" measures in hydrologic and hydroclimatic model
882        validation, Water Resources Res., 35, 233-241, 1999.

883    Linn, R., Reisner, J., Colman, J.J. and Winterkamp, J.: Studying wildfire behavior using FIRETEC. International journal of
884        wildland fire, 11(4), pp.233-246, 2002.

885    Lu, Z., and Sokolik, I.N.: Examining the impact of smoke on frontal clouds and precipitation during the 2002 Yakutsk
886        wildfires using the WRF-Chem-SMOKE model and satellite data, J. Geophys, Res. Atm., 122, 12765-12785,
887        https://doi.org/10.1002/2017JD027001, 2017.

888    Luig, A., Bofinger, S., Beyer, H.G.: Analysis of confidence intervals for the prediction of regional wind power output, Proc.
889        European    Wind    Energy    Conference,    Copenhagen,    pp    725-728,    2001.    Available    at
890        https://www.researchgate.net/publication/228793040_Analysis_of_confidence_intervals_for_the_prediction_of_region
891        al_wind_power_output, last accessed August 23, 2020.

Makar, P.A., Gong, W., Milbrandt, J., Hogrefe, C., Zhang, Y., Curci, G., Zabkar, R., Im, U., Balzarini, A., Baro, R., Bianconi, R., Cheung, P., Forkel, R., Gravel, S., Hirtl, H., Honzak, L., Hou, A., Jimenz-Guerrero, P., Langer, M., Moran, M.D., Pabla, B., Perez, J.L., Pirovano, G., San Jose, R., Tuccella, P., Werhahn, J., Zhang, J., Galmarini, S.: Feedbacks between air pollution and weather, part 1: Effects on weather. Atmospheric Environment, 115, 442-469, 2015a.

Makar, P.A., Gong, W., Hogrefe, C., Zhang, Y., Curci, G., Zabkar, R., Milbrandt, J., Im, U., Balzarini, A., Baro, R., Bianconi, R., Cheung, P., Forkel, R., Gravel, S., Hirtl, H., Honzak, L., Hou, A., Jimenz-Guerrero, P., Langer, M., Moran, M.D., Pabla, B., Perez, J.L., Pirovano, G., San Jose, R., Tuccella, P., Werhahn, J., Zhang, J., Galmarini, S.: Feedbacks between air pollution and weather, part 2: Effects on chemistry. Atmospheric Environment, 115, 499-526, 2015b.

Makar, P.A., Moran, M.D., Schultz, M.T., Taylor, A.: Speciation of volatile organic compound emissions for regional air quality modeling of particulate matter and ozone, J. Geophys. Res., 108, D2, 4041, doi:1029/2001JD000797, 2003.

Makar, P.A., Staebler, R.M., Akingunola, A., Zhang, J., McLinden, C., Kharol, S.K., Pabla, B., Cheung, P. and Zheng, Q.: The effects of forest canopy shading and turbulence on boundary layer ozone, Nature Communications, 8, art. no. 15243, doi: 10.1038/ncomms15243, 2017.

Makar, P.A., Stroud, C., Akingunola, A., Zhang, J., Ren, S., Cheung, P., and Zheng, Q.: Vehicle induced turbulence and atmospheric pollution, Proceedings of the National Academy of Sciences of the USA (under review), 2020.

Mallet, M., Solmon, F., Roblou, L., Peers, F., Turquety, S., Waquet, F., Jethva, H., Torres, O.: Simulation of optical properties and direct and indirect radiative effects of smoke aerosols over marine stratocumulus clouds during summer 2008 in California with the regional climate model RegCM, J. Geophys. Res. Atm., 122, 10312-10337, https://doi.org/10.1002/2107JD026905, 2017.

Mandel, J., Beezley, J.D., Kochanski, A.K., Coupled atmosphere-wildland fire modelling with WRF 3.3 and SFIRE 2011, Geosci. Model Dev., 4, 591-610, 2011.

Markowicz, K.M., Pakszys, R., Ritter, C., Zielensi, T., Udisti, R., Cappelletti, D., Mazzola, M., Shobara, M., Xian, P., Zawadzka, O., Lisok, J., Petelski, T., Makuch, P., Karasinksi, G.: Impact of North American intense fires on aerosol optical properties measured over the European Arctic in July 2015, J. Geophys. Res. Atm., 121, 14487-14512, doi:10.1002/2016JD025310, 2016.

Milbrandt, J.A. and Morrison, H.: Parameterization of Cloud Microphysics Based on the Prediction of Bulk Ice Particle Properties. Part III: Introduction of Multiple Free Categories. J. Atmos. Sci., 73, 975-995, doi: https://doi.org/10.1175/JAS-D-15-0204.1, 2016.

Milbrandt, J. A., S. Bélair, S., Faucher, M., Vallée, M., Carrera, M.L., and Glazer, A.:The pan-Canadian High Resolution (2.5 km) Deterministic Prediction System. Wea. Forecasting, 31, 1791-1816, 2016.

Milbrandt, J.A., and Yau, M.K: A multimoment bulk microphysics parameterization. Part 1: analysis of the role of the spectral shape parameter, J. Atmos. Sci., 62, 3051-3064, 2005a.

Milbrandt, J.A., and Yau, M.K: A multimoment bulk microphysics parameterization. Part II: a proposed three-moment closure and scheme, J. Atmos. Sci., 62, 3065-3081, 2005b

926 Moran, M.D., Pavlovic, R., and Anselmo, D.: Regional air quality deterministic prediction system (RAQDPS): update from
927   version   019   to   version   020,   Montreal,   available   at:
928   http://collaboration.cmc.ec.gc.ca/cmc/CMOI/product_guide/docs/tech_note/technote_raqdps-v2.0_20180918_e.pdf,
929   last access: 1 December 2018.

930 Morrison, H., and Milbrandt, J.A.: Parameterization of Cloud Microphysics Based on the Prediction of Bulk Ice Particle
931   Properties. Part I: Scheme Description and Idealized Tests. J. Atmos. Sci., 72, 287–311, doi: https://doi.org/10.1175/JAS-
932   D-14-0065.1, 2015.

933 Morrison, H. and W. W. Grabowski, W.W.: Modeling supersaturation and subgrid-scale mixing with two-moment warm
934   bulk microphysics. J. Atmos. Sci., 65, 792–812, doi: https://doi.org/10.1175/2007JAS2374.1, 2008.

935 Myhre, G., Shindell, D., Bréon, F.-M., Collins, W., Fuglestvedt, J., Huang, J., Koch, D., Lamarque, J.-F., Lee, D., Mendoza,
936   B., Nakajima, T., Robock, A., Stephens, G., Takemura, T. and Zhang, H.: Anthropogenic and Natural Radiative
937   Forcing. In: Climate Change 2013: The Physical Science Basis. Contribution of Working Group I to the Fifth Assessment
938   Report of the Intergovernmental Panel on Climate Change [Stocker, T.F., D. Qin, G.-K. Plattner, M. Tignor, S.K. Allen,
939   J. Boschung, A. Nauels, Y. Xia, V. Bex and P.M. Midgley (eds)). Cambridge University Press, Cambridge, United
940   Kingdom and New York, USA, 2013.

941 Nazarenko, L., Rind, D., Tsigaridis, K, Del Genio A.D, Kelly, M., and Tausnev, N.: Interactive nature of climate change and
942   aerosol forcing, J. Geophys. Res. Atm., 122, 3457-3480, doi:10.1002/2016JD025809, 2017.

943 Oeropoulis, L., Cho, N., and Lee, D.: A global survey of apparent aerosol-cloud interaction signals, J. Geophys. Res. Atm,
944   125, e2019JD031287, https://doi.org/10.1029/2019JD031287, 21pp, 2020.

945 O'Neill, N.T., Eck, T.G., Holben, B.N., Smirnov, A., Royer, A., and Li, Z.: Optical properties of boreal forest fire smoke
946   derived from Sun photometry, J. Goephys. Res., 107, 4125, doi 10.1029/2001JD000877, 21 pp., 2002

947 Palacios-Pena, L., Baro, R., Baklanov, A., Balzarini, A., Brunner, D., Forkel, R., Hirtl, M., Honzak, L., Lopez-Romero, J.M.,
948   Motavez, J.P., Perez, J.L., Pirovano, G., San Jose, R., Schroder, W., Werhahn, J., Wolke, R., Zabkar, R., and Jimenez-
949   Guerrero, P.: An assessment of aerosol optical properties from remote-sensing observations and regional chemistry-
950   climate coupled models over Europe, Atm. Chem. Phys., 18, 5021-5043, 2018.

951 Pan, L., Kim, H. C., Lee, P., Saylor, R., Tang, Y., Tong, D., Baker, B., Kondragunta, S., Xu, C., Ruminski, M. G., Chen, W.,
952   Mcqueen, J., and Stajner, I.: Evaluating a fire smoke simulation algorithm in the National Air Quality Forecast Capability
953   (NAQFC) by using multiple observation data sets during the Southeast Nexus (SENEX) field campaign, Geosci. Model
954   Dev. Discuss., https://doi.org/10.5194/gmd-2017-207, 2017.

955 Pavlovic, R., Chen, J., Anderson, K., Moran, M.D., Beaulieu, P.A., Davignon, D. and Cousineau, S.: The FireWork air quality
956   forecast system with near-real-time biomass burning emissions: Recent developments and evaluation of performance for
957   the 2015 North American wildfire season. Journal of the Air & Waste Management Association, 66(9), 819-841, 2016.

958 Peace, M., Mattner, T., Mills, G., Kepert, J., and McCaw, L., Fire-modified meteorology in a coupled fire-atmosphere model,
959   J. App. Met. and Clim., 54, 704-720, 2015.

960 Penner, J.E, Zhou, C., Garnier, A., Mitchell, D.L.: Anthropogenic aerosol indirect effects in cirrus clouds, J. Geophys. Res.
961     Atm., 123, 11652-11677, https://doi.org/10.1029/2018JD029204, 2018.

962 Pinson, P., and Kariniotakis, G.: On-line adaptation of confidence intervals based on weather stability for wind power
963     forecasting, in Proc. Of the Global Wind Power Conference, Chicago, USA, 2004. Available at https://hal-mines-
964     paristech.archives-ouvertes.fr/hal-00529488/document, last accessed August 23, 2020.

965 Pinto, J. O., Grim, J.A., Steinter, M.: Assessment of the High-Resolution Rapid Refresh model's ability to predict mesoscale
966     convective systems using object-based evaluation. J. Atmos. Sci., 30, 892-913, 2015.

967 Rothenberg, D., Avramov, A., Wang, C.: On the representation of aerosol activation and its influence on model-derived
968     estimates of the aerosol indirect effect, Atm. Chem. Phys., 18, 7961-7983, 2018.

969 Sandu, A. and Sander, R.: Technical note: Simulating chemical systems in Fortran90 and Matlab with the Kinetic
970     PreProcessor KPP-2.1, Atmos. Chem. Phys., 6, 187–195, https://doi.org/10.5194/acp-6-187-2006, 2006

971 Saponaro, G., Kolmonen, P., Sogacheva, L., Rodriguez, E., Virtanen, T., and de Leeuw, G.: Estimates of the aerosol indirect
972     effect over the Baltic Sea region derived from 12 years of MODIS observations, Atm. Chem. Phys., 17, 3133-3143,
973     2017.

974 Seity, Y., Brousseau, P., Malardel, S., Hello, G., Bénard, P., Bouttier, F., Lac, C., and Masson, V.: The AROME-France
975     convective-scale operational model. Mon. Wea. Rev., 139, 876-913, 2010.

976 Stockwell, W.R. and Lurmann, F.W.: Intercomparison of the ADOM and RADM gas-phase chemical mechanisms, Electric
977     Power Institute Topical Report, Electric Power Institute, Palo Alto, California, 323pp, 1989.

978 Stroud, C.A., Makar, P.A., Zhang, J., Moran, M.D., Akingunola, A., Li, S.-M., Leithead, A., Hayden, K., Siu, M.: Improving
979     air quality model predictions of organic species using measurement-derived organic gaseous and particle emissions in a
980     petrochemical-dominated region. *Atmospheric Chemistry and Physics*, 18 (18), pp. 13531-13545, 2018.

981 Sundqvist, H.: Parameterization of condensation and associated clouds in models for weather prediction and general
982     circulation simulation. In: Schlesinger M.E. (eds) Physically-Based Modelling and Simulation of Climate and Climatic
983     Change. NATO ASI Series (Series C: Mathematical and Physical Sciences), vol 243. Springer, Dordrecht, 1988.

984 Suzuki, K, and Takemura, T.: Perturbations to global energy budget due to absorbing and scattering aerosols, J. Geophys.
985     Res. Atm., 124, 2194-2209, https://doi.org/10.1029/2018JD029808, 2019.

986 Takeishi, A., Strorelvmo, T., and Fierce, L.: Disentangling the microphysical effects of fire particles on convective clouds
987     through a case study, J. Geophys. Res. Atm., doi:10.1029/2019JD031890, 2020.

988 Twomey, S.: The influence of polution on the shortwave albedo of clouds, J. Atmos. Sci, 34, 1149-1152, 1977.

989 Wang, J., Allen, D.J., Pickering, K.E., Li, Z., and He, H.: Impact of aerosol direct effect on East Asian air quality during the
990     EAST-AIRE campaign, J. Geophys. Res. Atm., 121, 6534-6554, doi:10.1002/2016JD025108, 2016.

991 Whaley, C.H., Makar, P.A., Shephard, M.W., Zhang, L., Zhang, J., Zheng, Q., Akingunola, A., Wentworth, G.R., Murphy,
992     J.G., Kharol, S.K., and Cady-Periera, K.E.: Contributions of natural and anthropogenic sources to ambient ammonia in
993     the Athabasca oil sands and north-western Canada, Atm. Chem. Phys., 18, 2011-2034, 2018.

994      Willmott, C.J., Robeson, S.M., Matsuura, K., A refined index of model performance, Int. J. Climatol., 32, 2088-2094, 2012.

995      Yu, S., Eder, B., Dennis, R., Chu, S.-H., Schwartz, S.E., New unbiased metrics for evaluation of air quality models, Atmos.
996          Sci. Let., 7, 26-34, 2006.

997      Zhang, L., Brook, J.R., and Vet., R.: A revise parameterization for gaseous dry deposition in air-quality models, Atm. Chem.
998          Phys., 3, 2067-2082, https://doi.org/10.5194/acp-3-2067-2003, 2003.

999      Zhao, X., Liu, Y., Yu, F., and Heidinger, A.K.: Using long-term satellite observations to identify sensitive regimes and active
1000         regions of aerosol indirect effects for liquid clouds over global oceans, J. Geophys. Res. Atm., 123, 457-472,
1001         https://doi.org/10.1002/2017JD027187, 2018.

1002      Zhu, J., and Penner, J.E.: Indirect effects of secondary organic aerosol on cirrus clouds, J. Geophys., Res. Atm., 125,
1003         e2019JD032233, https://doi.org/10.1029/2019JD032233, 19 pp., 2020.

1004

1005

**Tables:**

| Model Process or Configuration Component | Description | Reference (where applicable) |
|---|---|---|
| Base weather forecast model | Global Environmental Multiscale (GEM), v4.9.8 | Cote *et al*. (1998), Girard *et al*. (2014) |
| Base air-quality model | Global Environmental Multiscale – Modelling Air-quality and Chemistry (GEM-MACH) v2 | Moran *et al*. (2018) |
| Aerosol Direct Effect | Feedback simulations: GEM-MACH's predicted aerosol loading and Mie scattering using a binary water-dry aerosol homogeneous mixture assumption, at 4 wavelengths employed by GEM's radiative transfer algorithms, and at additional wavelengths for diagnostic purposes.<br><br>No-Feedback simulations: invariant climatological values for aerosol optical properties are used. | Makar *et al*. (2015a,b) |
| Aerosol Indirect Effect | Feedback simulations: Modified P3 cloud microphysics scheme, driven by an aerosol size and speciation specific nucleation scheme (Abdul-Razzak and Ghan, 2002).<br><br>No-feedback implementation: P3 scheme driven by an invariant aerosol population of a single lognormal size distribution (with a geometric mean diameter of 100 nm and total aerosol number of 300 $cm^{-3}$ consisting of pure ammonium sulphate).<br><br>The prognostic cloud droplet number and mass mixing ratios from the P3 microphysics are then transferred back to the chemistry module for using in cloud processing of gases and aerosols (cloud scavenging and chemistry) calculations, completing the AIE feedback process loop in the case of the feedback implementation (Gong *et al.,* 2015). | Gong *et al*. (2015), Abdul-Razzak and Ghan (2002), Morrison and Milbrandt (2015), Milbrandt and Morrison (2016), Morrison and Grabowski (2008). |

| | | |
|---|---|---|
| Forest fire plume rise | CFFEPSv4.0 (see text) | |
| Gas-phase chemistry mechanism | ADOMII mechanism, 42 gas species. | Stockwell *et al.* (1989) |
| Gas-Phase chemistry solver | KPP-generated RODAS3 solver | Sandu and Sander (2006) |
| Cloud processing of aerosols | Aqueous chemistry, scavenging of gases and aerosols, below-cloud removal and wet deposition. | Gong *et al.* (2015) |
| Particle microphysics | Sectional size distribution and 8 chemical species. | Gong *et al.* (2003) |
| Particle inorganic thermodynamics | Local equilibrium subdomain approach | Makar *et al.* (2003) |
| Secondary organic aerosol formation | Modified yield approach | Stroud *et al.* (2018) |
| Vertical diffusion | Fully implicit approach, with surface fluxes as a boundary condition | |
| Advection | Semi-Lagrangian approach, 3-shell mass conservation correction (ILMC approach) | |
| Forest canopy shading and turbulence. | Light attenuation within forest canopies and turbulence reductions due to vegetation applied to thermal coefficients of diffusivity. | Makar *et al.* (2017) |
| Anthropogenic plume rise | Parameterization calculating residual buoyancy of the rising plume. | Akingunola *et al.* (2018). |
| Meteorological modulation of aerosol crustal material | Aerosol crustal material is inhibited when the soil water content is > 10%. | |

| Ammonia emissions and deposition | Bi-directional flux parameterization employed. | Whaley *et al.* (2018), Zhang *et al.* (2003). |
|---|---|---|
| Methane treatment | Reactive, emitted and transported tracer | |
| Leaf Area Index data | MODIS retrievals used to create monthly LAI values for biogenic emissions, forest canopy shading and turbulence, deposition | |
| Vehicle-induced turbulence | Observation-based parameterization used to modify near-surface coefficients of thermal diffusivity | Makar *et al.* (2020) |

1008

1009 **Table 1. GEM-MACH model configuration details and references.**
1010

| Event Forecast | Event Observed | |
|---|---|---|
| | Yes | No |
| Yes | A | B |
| No | C | D |

1011
1012 **Table 2. Event versus non-event contingency table. A = number of events forecast and observed; B=number of events forecast but**
1013 **not observed; C=number of events observed but not forecast; D = number of cases where events were neither forecast nor observed.**
1014

34

| Chemical | Region | Simulation | FO2 | MB | MGE | NMGE | R | RMSE | COE | IOA |
|---|---|---|---|---|---|---|---|---|---|---|
| **PM2.5** | Western Canada | No Feedback | 0.412 | 4.805 | 6.688 | 1.322 | **0.259** | 10.163 | -1.476 | -0.192 |
| | | Feedback | **0.414** | **4.578** | **6.531** | **1.291** | 0.238 | **9.803** | **-1.418** | **-0.173** |
| | Western USA | No Feedback | 0.556 | 1.953 | 5.349 | 0.823 | **0.254** | 8.571 | -0.538 | 0.231 |
| | | Feedback | 0.556 | **1.805** | **5.287** | **0.813** | 0.252 | **8.443** | **-0.520** | **0.240** |
| **O$_3$** | Western Canada | No Feedback | 0.741 | 5.988 | 11.089 | 0.495 | *0.527* | 15.445 | -0.223 | 0.388 |
| | | Feedback | **0.745** | **5.891** | **10.969** | **0.490** | *0.527* | **15.268** | **-0.210** | **0.395** |
| | Western USA | No Feedback | 0.865 | **1.731** | 10.702 | 0.285 | 0.693 | 14.279 | 0.249 | 0.625 |
| | | Feedback | **0.866** | 1.770 | **10.663** | **0.284** | **0.694** | **14.225** | **0.252** | **0.626** |
| **NO$_2$** | Western Canada | No Feedback | 0.437 | **-0.997** | **2.757** | **0.594** | 0.564 | 3.965 | 0.154 | *0.577* |
| | | Feedback | **0.429** | -1.037 | 2.758 | 0.595 | **0.565** | **3.936** | 0.154 | *0.577* |
| | Western USA | No Feedback | **0.493** | **-0.346** | 2.341 | 0.572 | **0.653** | 3.674 | 0.177 | 0.588 |
| | | Feedback | 0.483 | -0.427 | **2.332** | **0.570** | 0.651 | **3.657** | **0.180** | **0.590** |

Table 3: Summary performance metrics for ozone, nitrogen dioxide, and PM2.5. Bold-face indicates the simulation with the better performance score for the given metric, chemical species and sub-region, italics indicate a tied score, and regular font the simulation with the lower performance score. FO2: fraction of scores within a factor of 2. MB: Mean Bias. MGE: Mean Gross Error. NMGE: Normalized Mean Gross Error. R: Correlation Coefficient. RMSE: Root Mean Square Error. COE: Coefficient of Error. IOA: Index of Agreement.
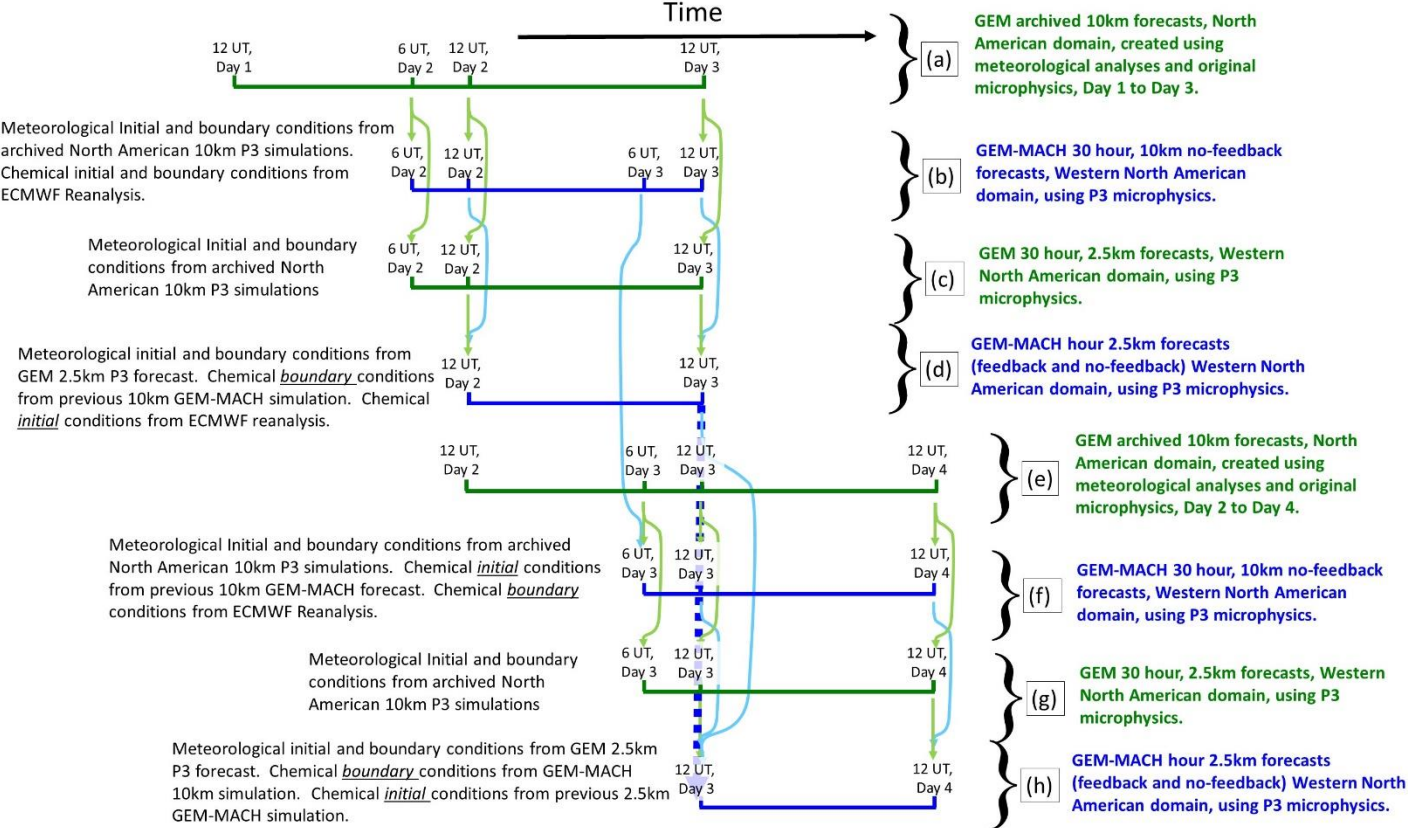
1023

1024  **Figures:**

1025
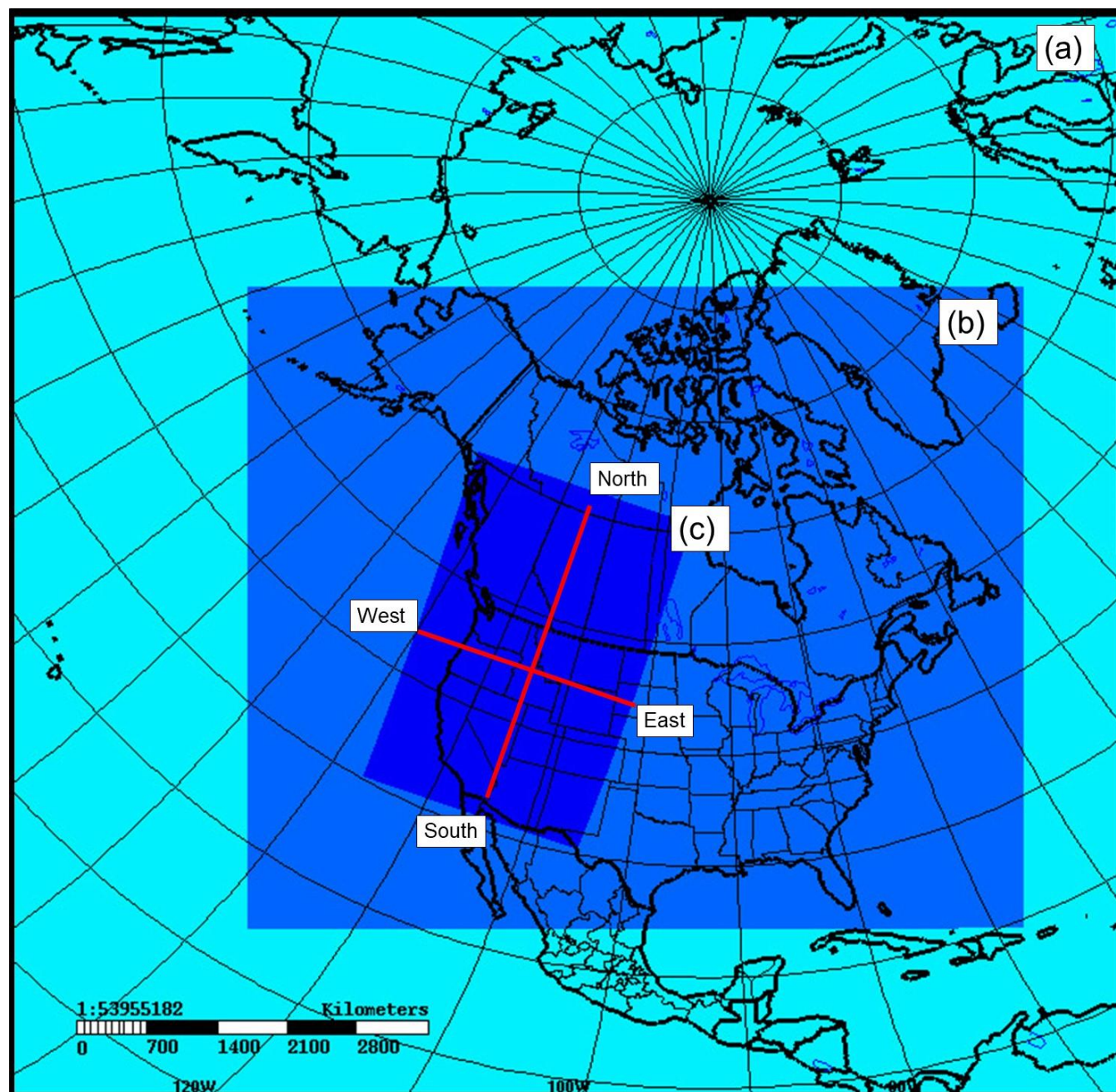


1026

1027  **Figure 1: GEM-MACH domains: (a) GEM meteorology 10km resolution forecast domain. (b) GEM-MACH 10km resolution**
1028  **forecast domain. (c) GEM-MACH inner 2.5-km grid resolution forecast domain for comparison to observations. Red lines indicate**
1029  **locations of illustrative South to North and West to East cross-sections appearing in subsequent analysis in the text.**

Time

GEM archived 10km forecasts, North American domain, created using meteorological analyses and original microphysics, Day 1 to Day 3.

Meteorological Initial and boundary conditions from archived North American 10km P3 simulations. Chemical initial and boundary conditions from ECMWF Reanalysis.

GEM-MACH 30 hour, 10km no-feedback forecasts, Western North American domain, using P3 microphysics.

Meteorological Initial and boundary conditions from archived North American 10km P3 simulations

GEM 30 hour, 2.5km forecasts, Western North American domain, using P3 microphysics.

Meteorological initial and boundary conditions from GEM 2.5km P3 forecast. Chemical *boundary* conditions from previous 10km GEM-MACH simulation. Chemical *initial* conditions from ECMWF reanalysis.

GEM-MACH hour 2.5km forecasts (feedback and no-feedback) Western North American domain, using P3 microphysics.

GEM archived 10km forecasts, North American domain, created using meteorological analyses and original microphysics, Day 2 to Day 4.

Meteorological Initial and boundary conditions from archived North American 10km P3 simulations. Chemical *initial* conditions from previous 10km GEM-MACH forecast. Chemical *boundary* conditions from ECMWF Reanalysis.

GEM-MACH 30 hour, 10km no-feedback forecasts, Western North American domain, using P3 microphysics.

Meteorological Initial and boundary conditions from archived North American 10km P3 simulations

GEM 30 hour, 2.5km forecasts, Western North American domain, using P3 microphysics.

Meteorological initial and boundary conditions from GEM 2.5km P3 forecast. Chemical *boundary* conditions from GEM-MACH 10km simulation. Chemical *initial* conditions from previous 2.5km GEM-MACH simulation.

GEM-MACH hour 2.5km forecasts (feedback and no-feedback) Western North American domain, using P3 microphysics.

Figure 2: Example time sequencing of model simulations used to generate the 2.5-km GEM-MACH simulations carried out here. Green lines and print indicate GEM (weather forecast only) simulations), blue lines and print indicate 2.5-km GEM-MACH simulations. Arrows indicate data flow (light green: meteorological information; light blue: chemical information). Steps (a) through (h) illustrate the sequence of forecasts used to generate two consecutive days of 2.5km GEM-MACH simulations. Note that on-line coupling occurs only at the 2.5km GEM-MACH forecast level, in this sequencing.
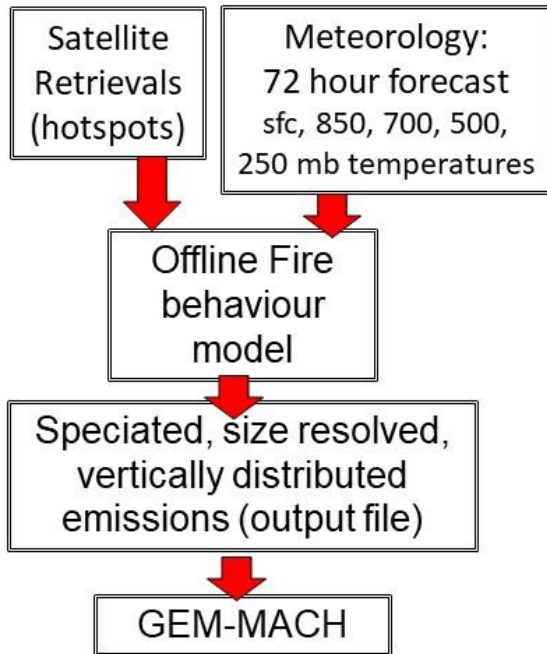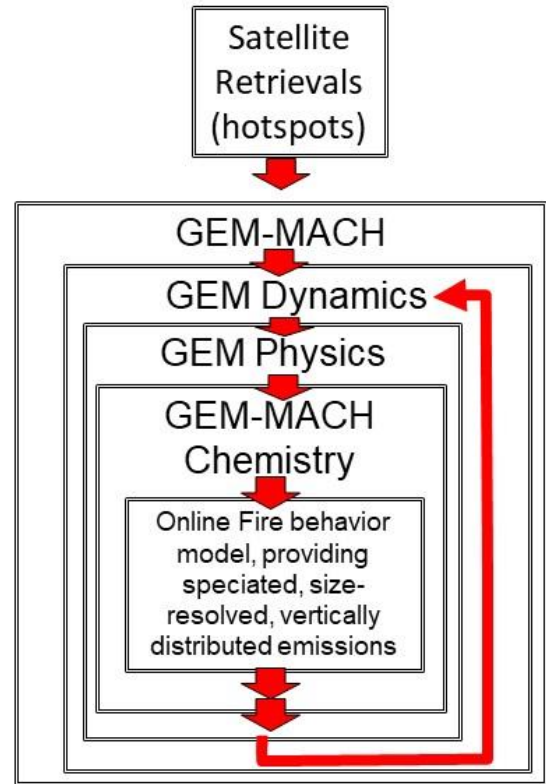
**Figure 3:** **Process comparison between original (CFFEPSv2.03, left) and on-line (CFFEPSv4.0, right) forest fire emissions and vertical plume distribution algorithms.**

1043
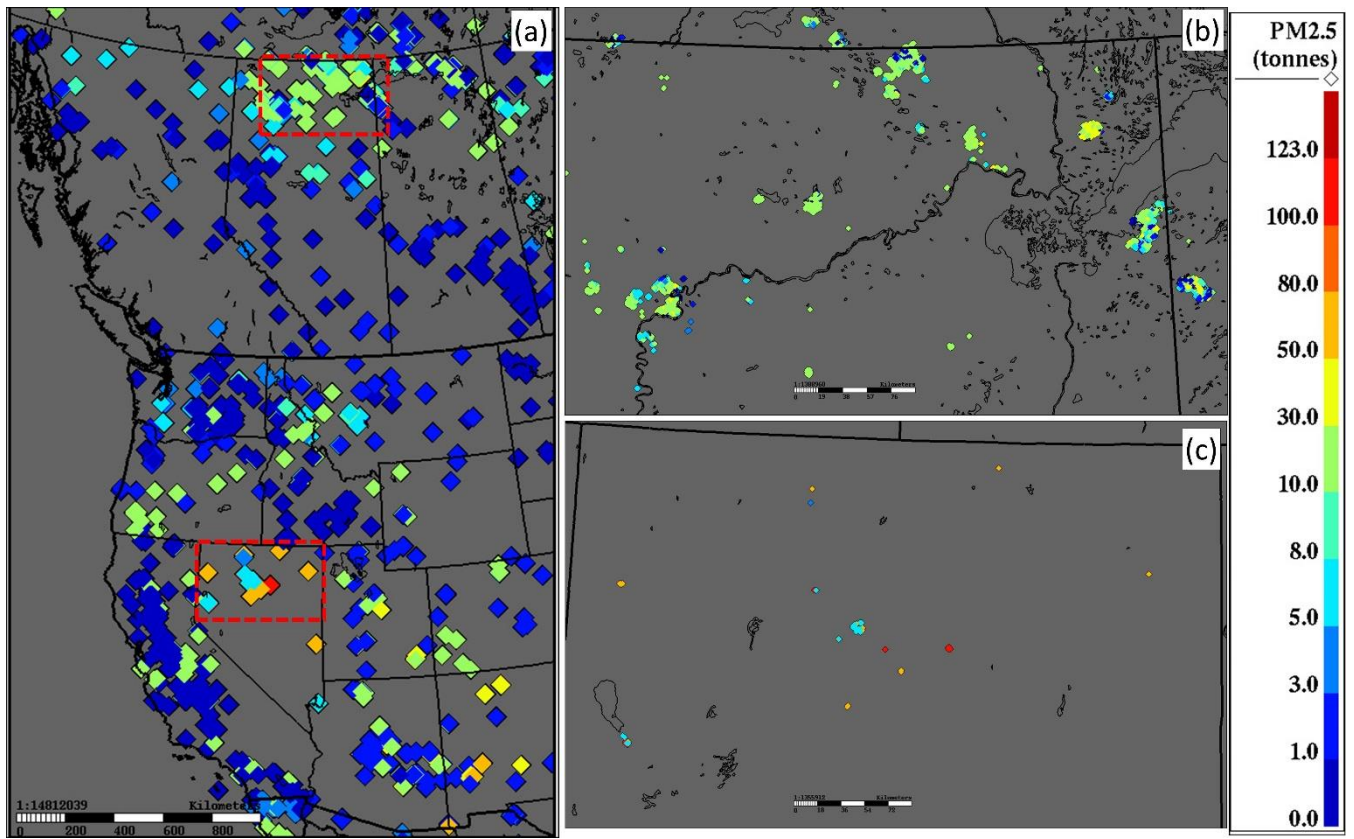
Figure 4: Hotspot locations during the study period, colour-coded by daily total tonnes PM2.5 emitted. (a) Entire model 2.5-km domain, with northern Alberta and northern Nevada sub-regions as red dashed boxes; (b) northern Alberta zoom, with smaller symbols for individual hotspots showing the large fire regions; (c) northern Nevada zoom, to the same scale as (b), showing isolated hotspots with high emissions.
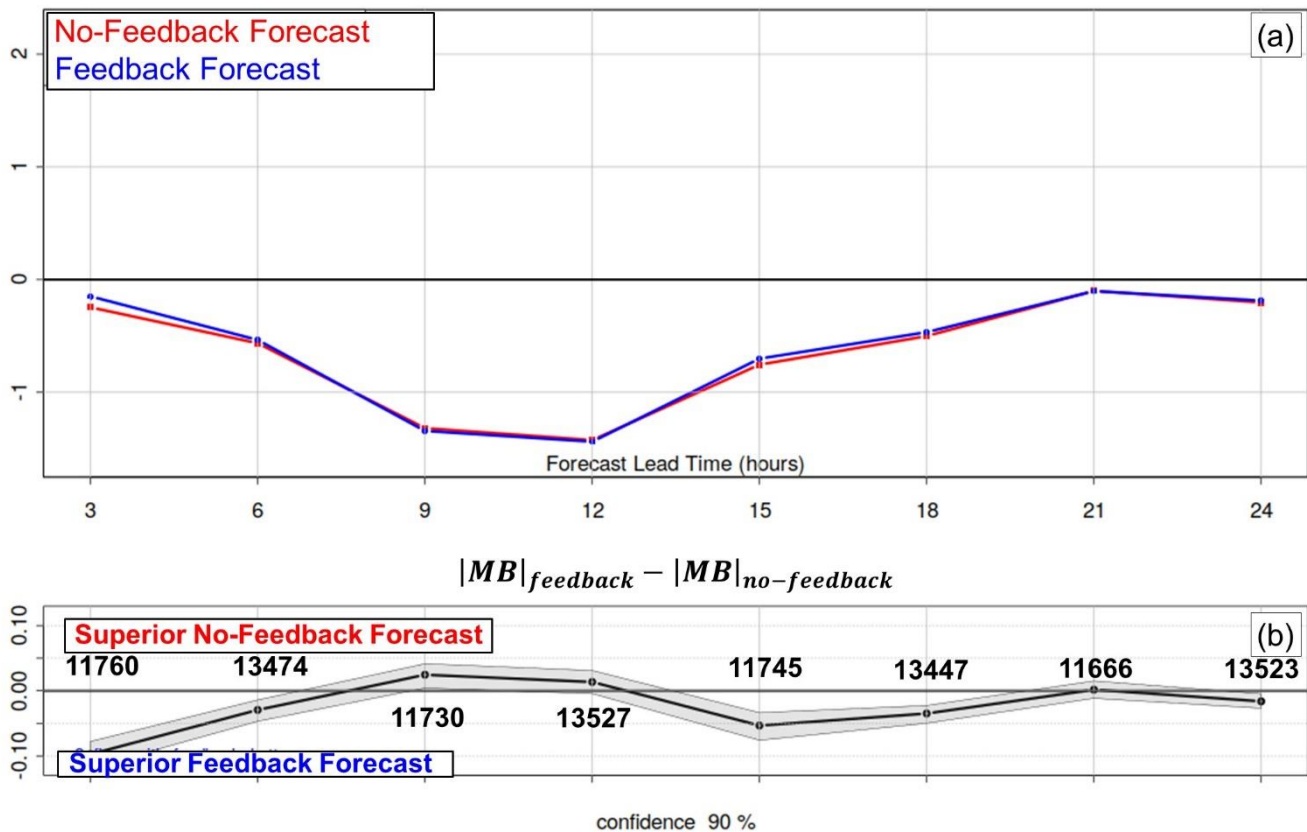
Figure 5: Mean bias in surface temperature (°C) at forecast hours starting at 0 UT. (a) Red line: no-feedback forecast values; blue line: feedback forecast values. (b) Difference in absolute value of mean bias between the two forecasts $\left(|MB|_{feedback} - |MB|_{no-feedback}\right)$, with the region *below* 90% confidence level shown shaded grey. Mean values above above/below the '0' line, and outside of the shaded region thus indicate differences in the mean between the two forecasts which differ at or above the 90% confidence level. Values of the difference which appear below/above the zero line and outside of the grey area thus indicate superior domain average performance for the feedback/no-feedback forecasts at each of the 3-hourly intervals, respectively. Numbers appearing above the metric differences are the number of observations contributing to the calculated metrics.

$$|MB|_{feedback} - |MB|_{no-feedback}$$

$$MAE_{feedback} - MAE_{no-feedback}$$

$$RMSE_{feedback} - RMSE_{no-feedback}$$

$$R_{no-feedback} - R_{feedback}$$
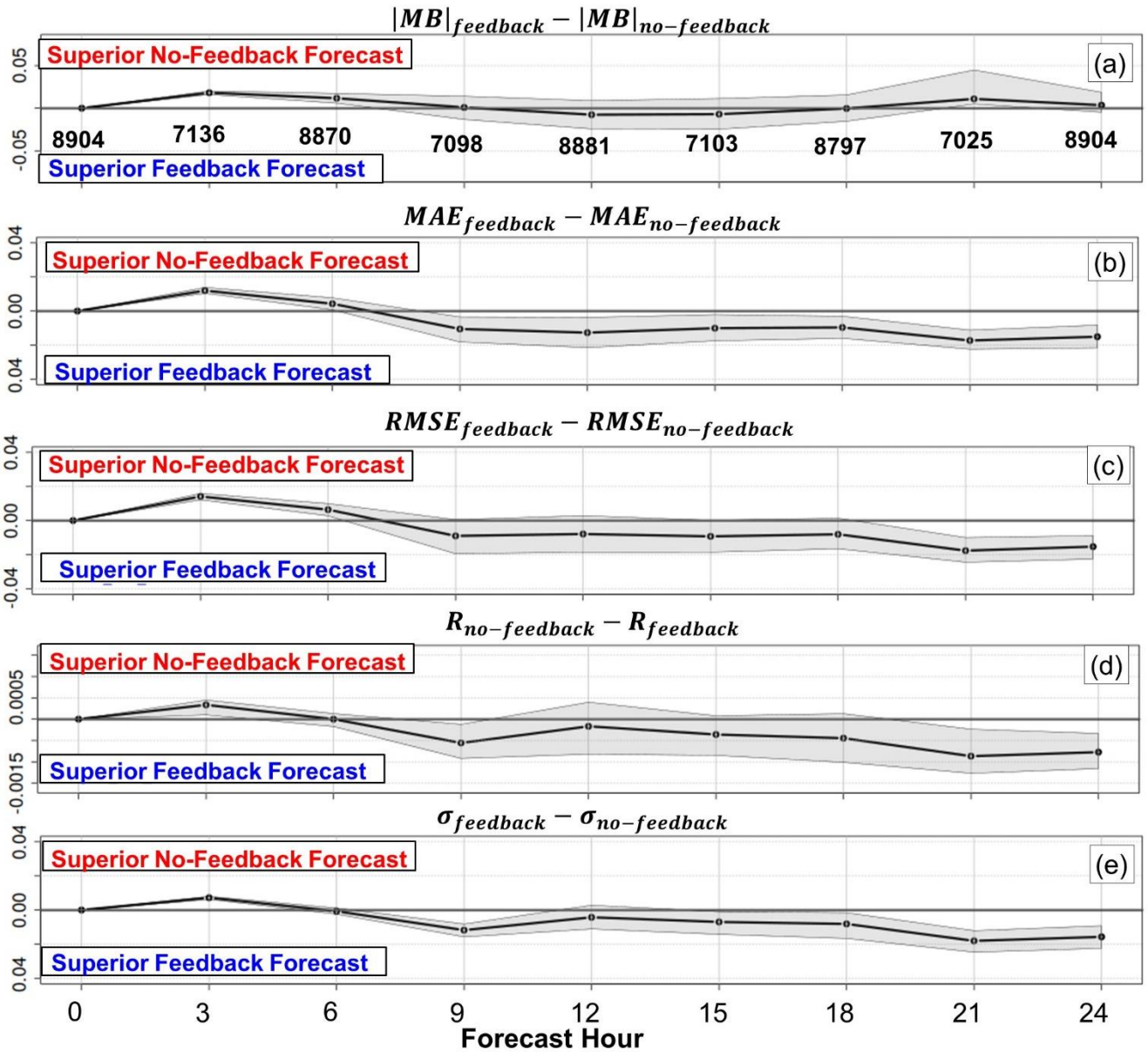
**Forecast Hour**
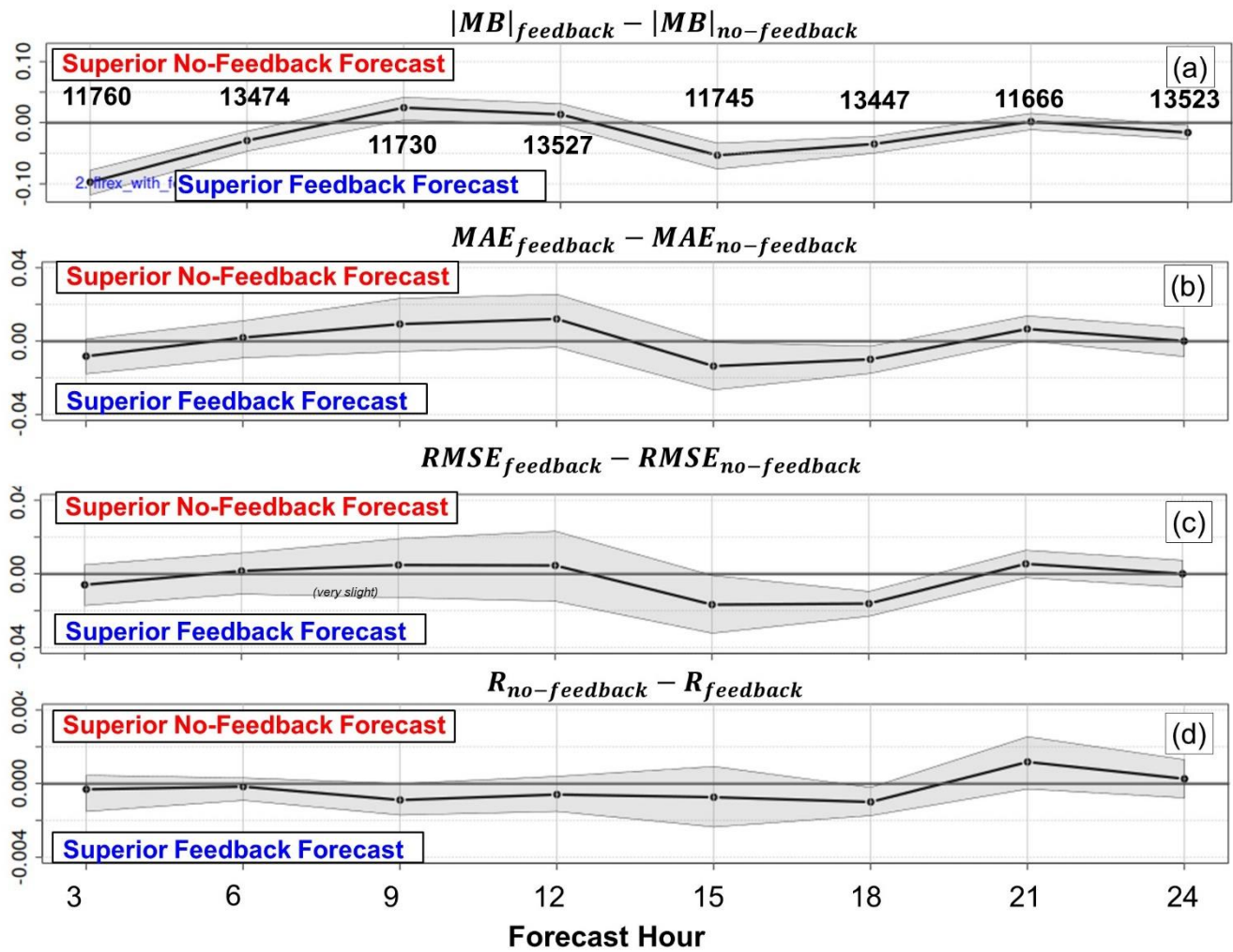
1058
1059 **Figure 6: Summary meteorological performance comparison for surface temperature (C). (a) mean bias, (b) mean absolute error,**
1060 **(c) root mean square error and (d) Pearson correlation coefficient. 90% confidence level shown in grey. Numbers appearing above**
1061 **the absolute mean bias differences are the number of stations contributing to the calculated metrics.**

41
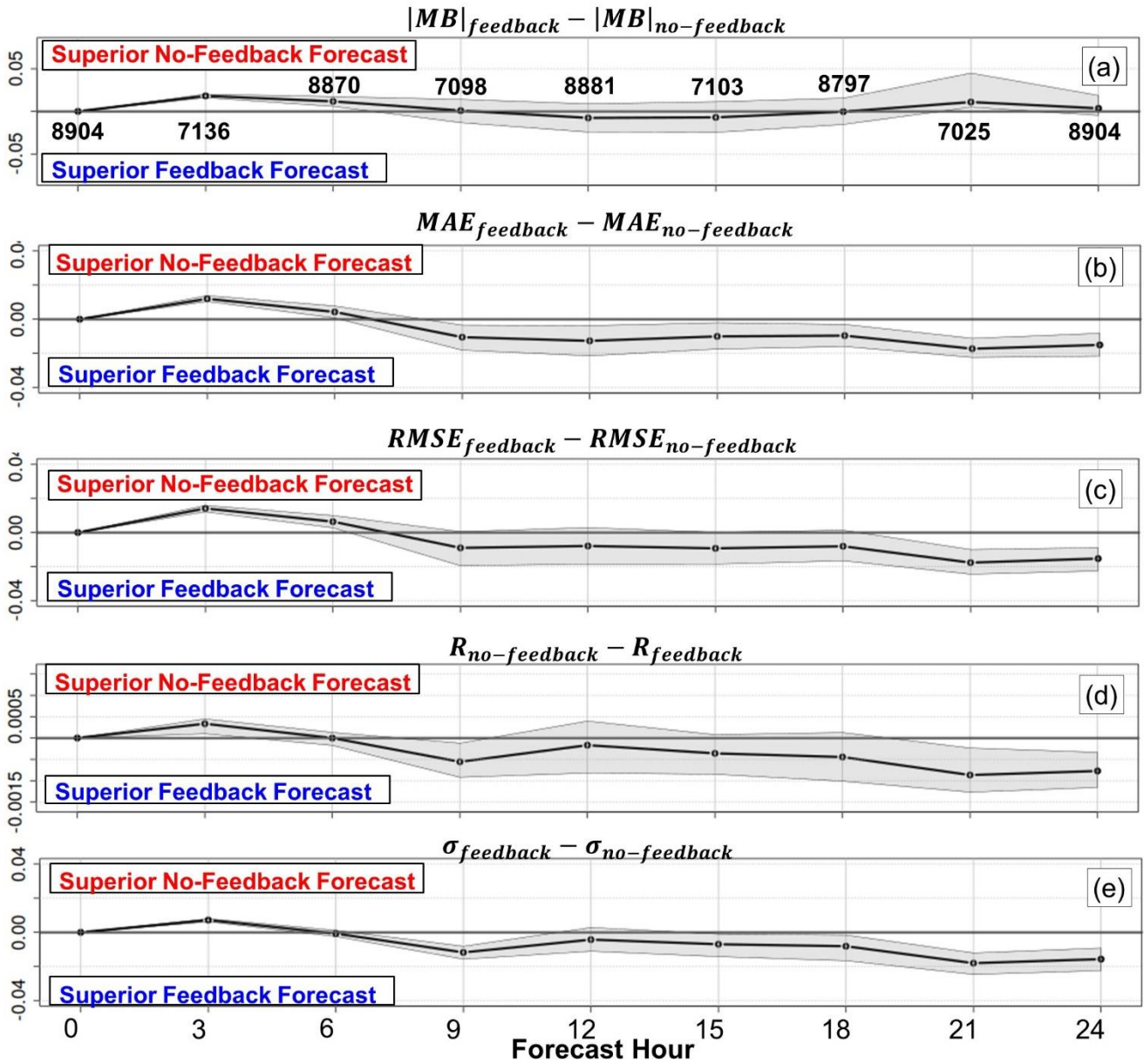
Figure 7: Summary meteorological performance comparison for surface pressure (hPa). (a) mean bias, (b) mean absolute error, (c) root mean square error, (d) Pearson correlation coefficient, and (e) standard deviation. 90% confidence level shown in grey. Numbers appearing above the absolute mean bias differences are the number of stations contributing to the calculated metrics.
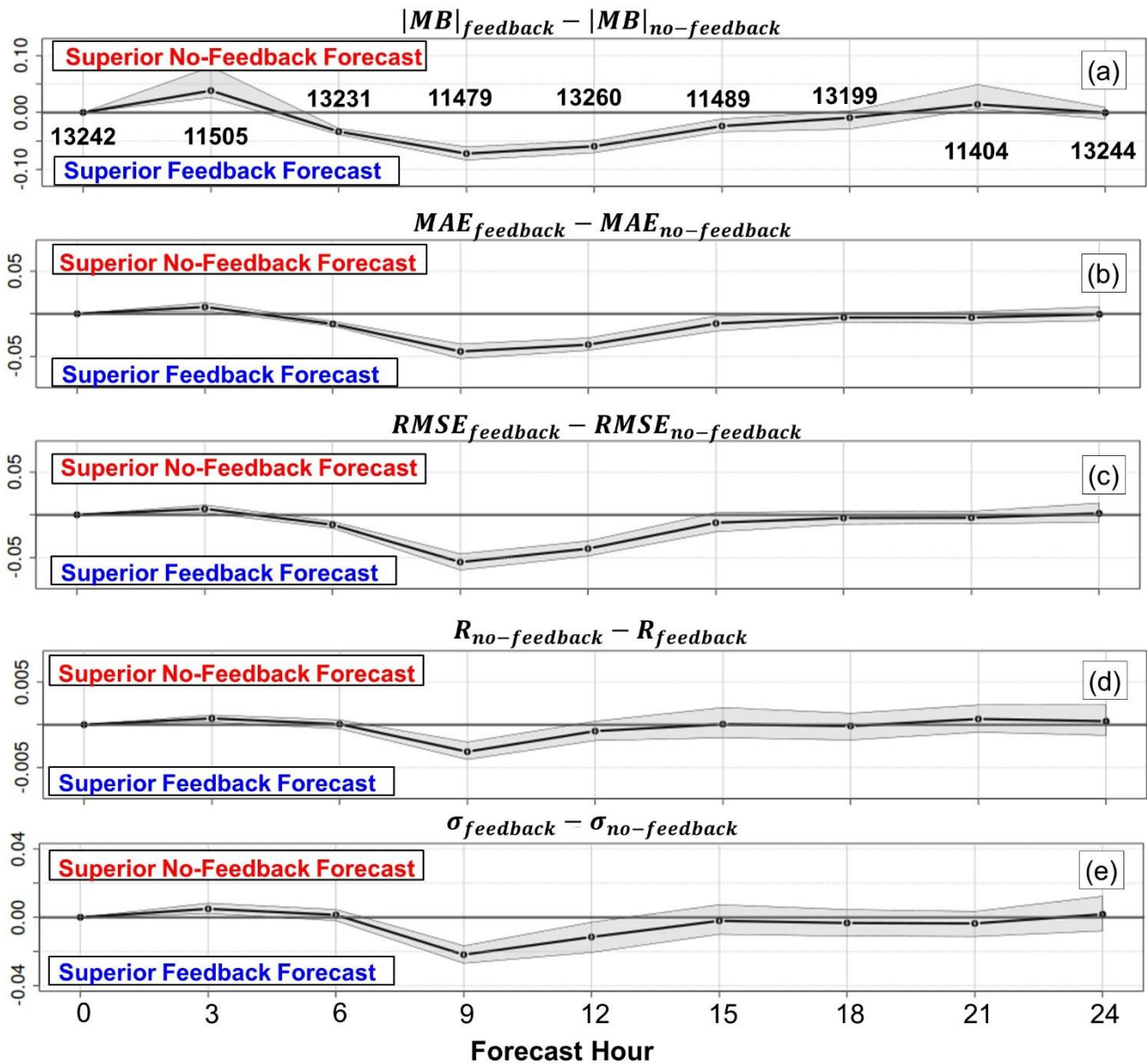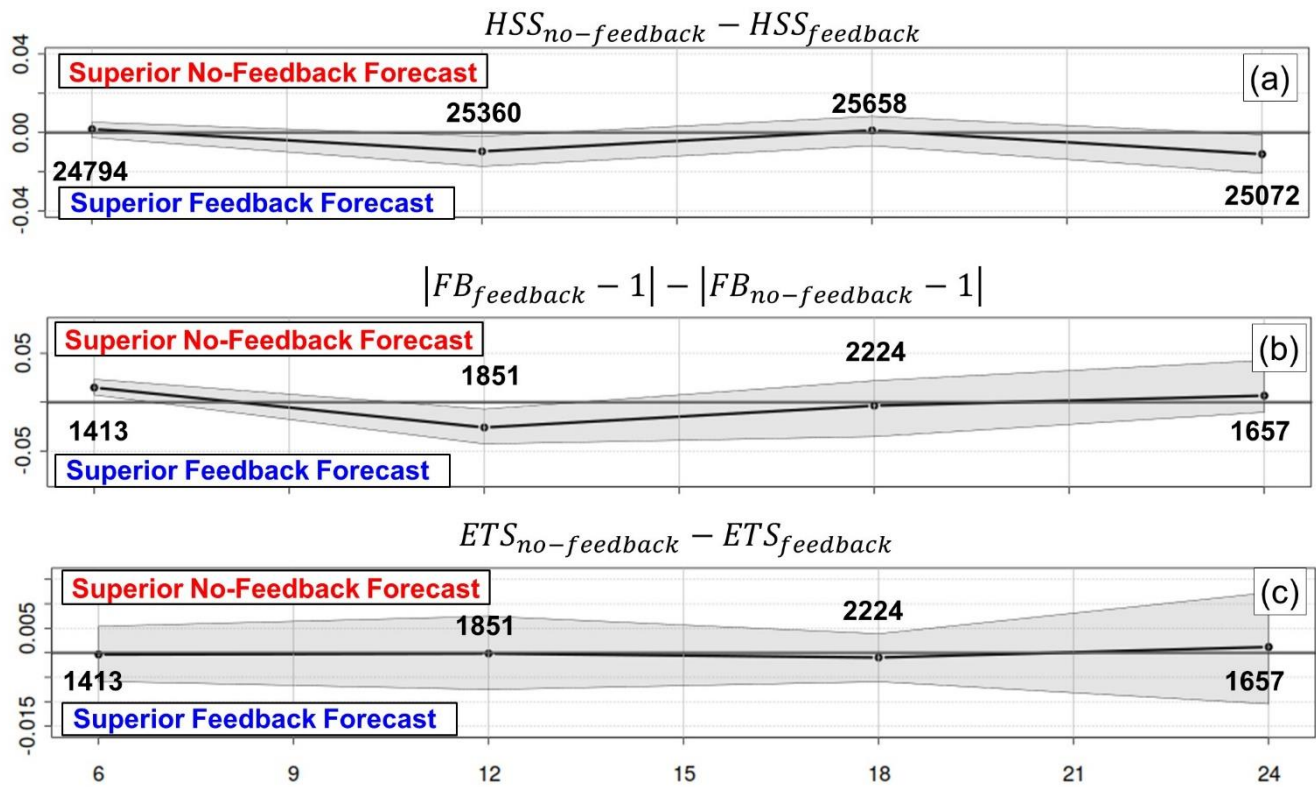
**Figure 8:** Summary meteorological performance comparison for dewpoint temperature (C). (a) mean bias, (b) mean absolute error, (c) root mean square error, (d) Pearson correlation coefficient, and (e) standard deviation. 90% confidence level shown in grey. Numbers appearing above the absolute mean bias differences are the number of stations contributing to the calculated metrics.

Figure 9: Summary meteorological performance comparison for sea-level pressure (hPa). (a) mean bias, (b) mean absolute error, (c) root mean square error, (d) Pearson correlation coefficient, and (e) standard deviation. 90% confidence level shown in grey. Numbers appearing above the absolute mean bias differences are the number of stations contributing to the calculated metrics.
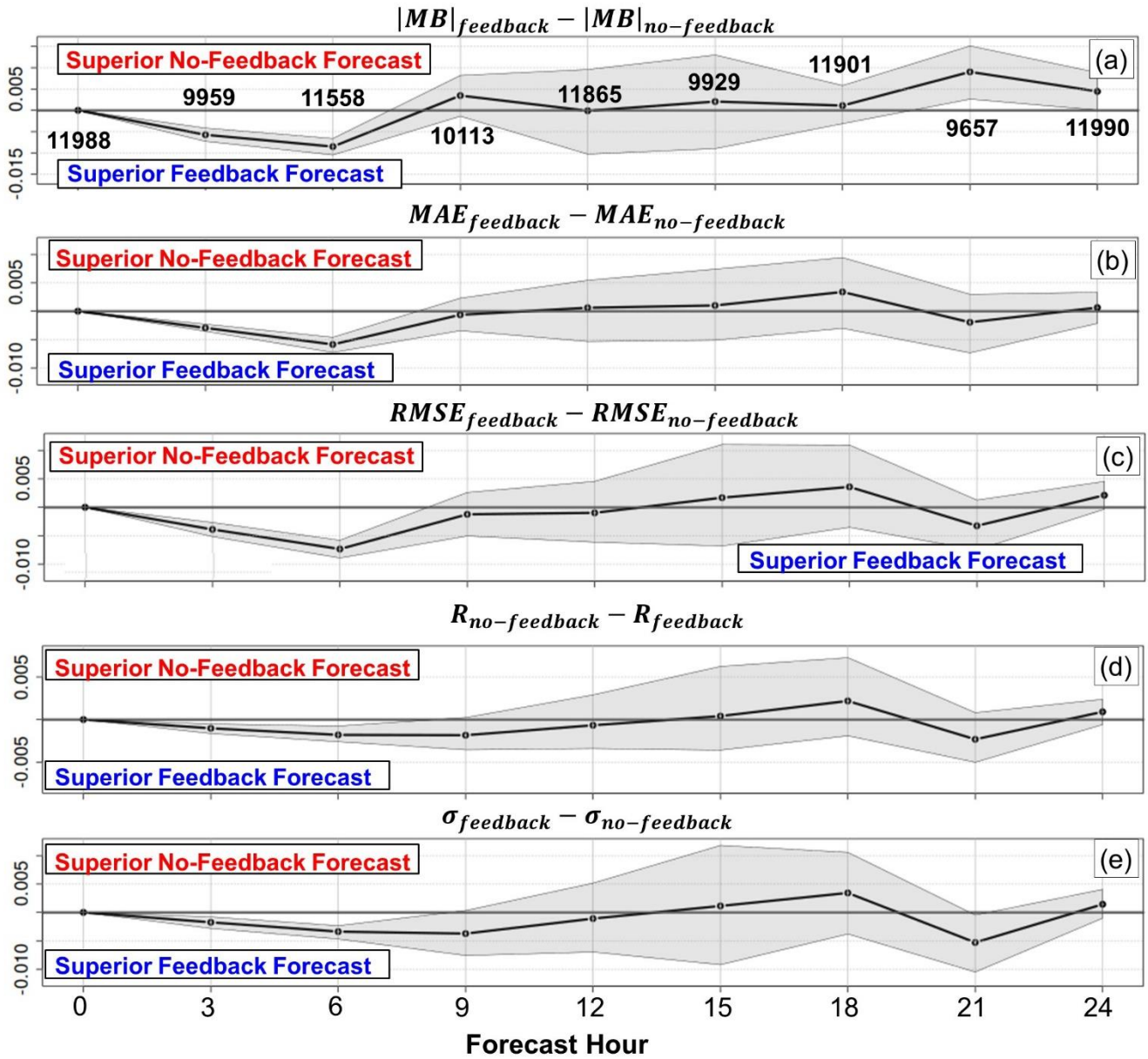
Figure 10: Summary meteorological performance comparison for 10m windspeed (m s$^{-1}$). (a) mean bias, (b) mean absolute error, (c) root mean square error, (d) Pearson correlation coefficient, and (e) standard deviation. 90% confidence level shown in grey. Numbers appearing above the absolute mean bias differences are the number of stations contributing to the calculated metrics.

$$HSS_{no-feedback} - HSS_{feedback}$$

**Superior No-Feedback Forecast**

**25360**    **25658**    (a)

**24794**

**Superior Feedback Forecast**    **25072**

$$\left|FB_{feedback} - 1\right| - \left|FB_{no-feedback} - 1\right|$$

**Superior No-Feedback Forecast**

**1851**    **2224**    (b)

**1413**

**Superior Feedback Forecast**    **1657**

$$ETS_{no-feedback} - ETS_{feedback}$$

**Superior No-Feedback Forecast**

**1851**    **2224**    (c)

**1413**

**Superior Feedback Forecast**    **1657**

1081
1082 **Figure 11: Precipitation performance evaluation (mm precipitation). (a) Heike skill score of 6-hour accumulated precipitation (No-**
1083 **Feedback – Feedback). (b) Frequency bias index of 6-hour accumulated precipitation (threshold of 2 mm, No-Feedback – Feedback).**
1084 **(c) Equitable Threat Score of 6-hour accumulated precipitation (threshold of 2 mm, No-Feedback – Feedback).**
1085

46

$|MB|_{feedback} - |MB|_{no-feedback}$  $MB_{feedback}, MB_{no-feedback}$
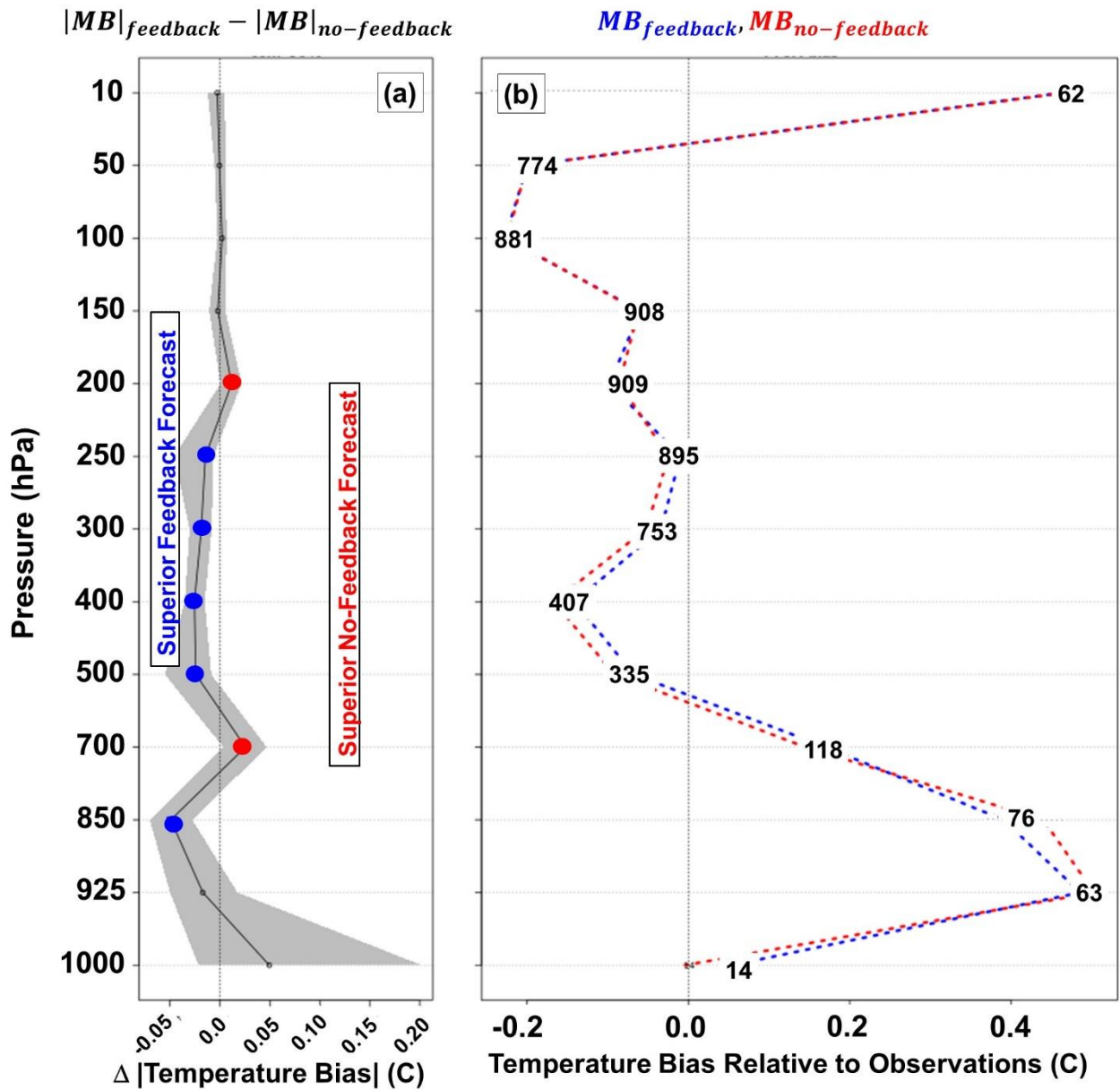
**Figure 12:** Forecast hour 12 (0 UT) summary upper air temperature performance comparison for air temperature (mean bias, C). (a) Difference in absolute value of mean bias in temperature, (feedback forecast – no-feedback forecast). Grey regions represent 90% confidence levels, blue symbols: pressure levels at which the feedback mean bias outperforms the no-feedback mean-bias at > 90% confidence. Red symbols: pressure levels at which the no-feedback mean bias outperforms the feedback mean bias at >90% confidence. 90% confidence level shown in grey. (b) Mean bias in upper air temperature for feedback (blue) and no-feedback (red) (C). Numbered values on the profiles indicate the number of observed data-model pairs at each pressure level.
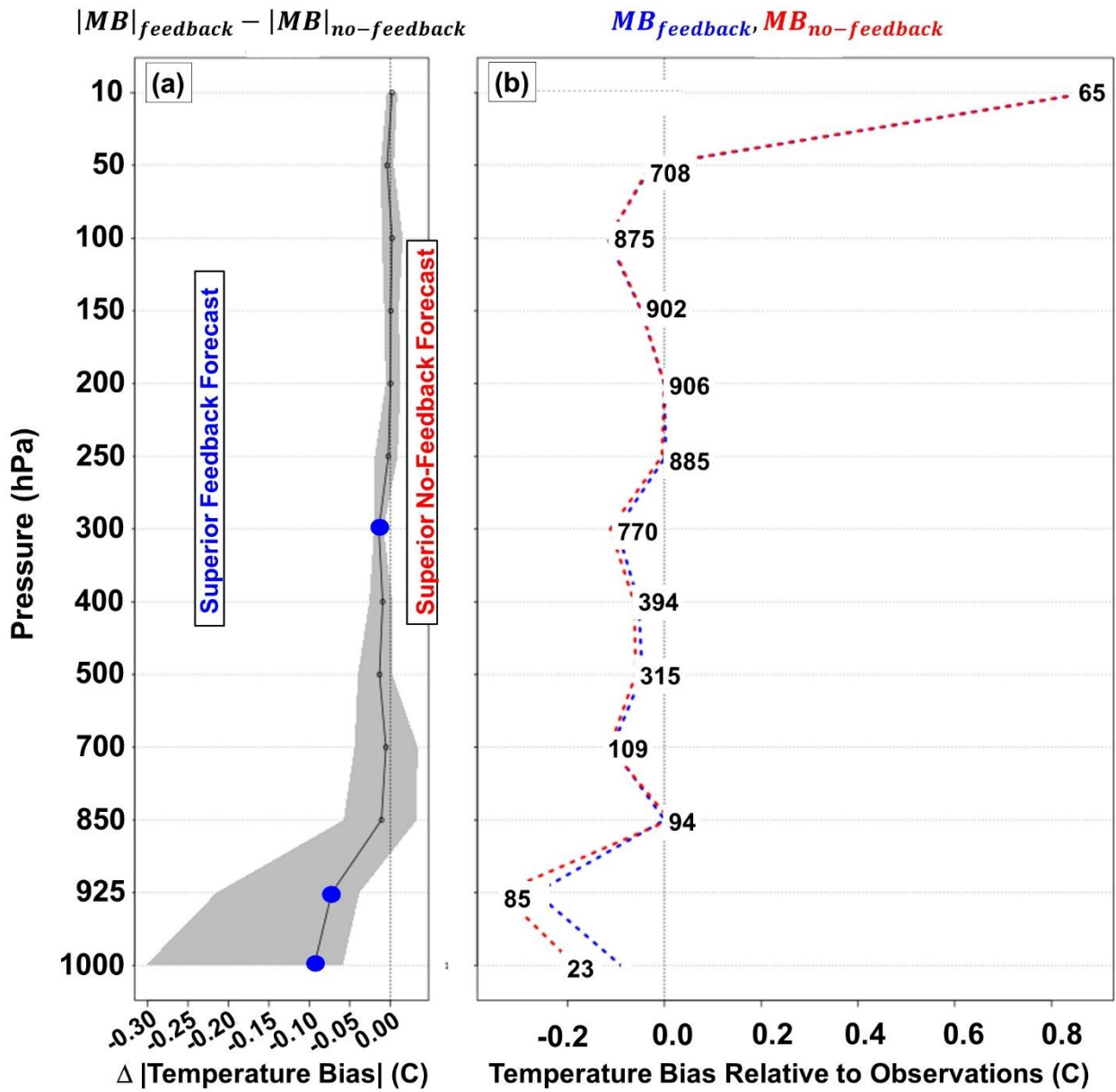
Figure 13: Forecast hour 24 (12 UT) summary upper air temperature performance comparison for air temperature (mean bias, C). (a,b) as in Figure 12.

48
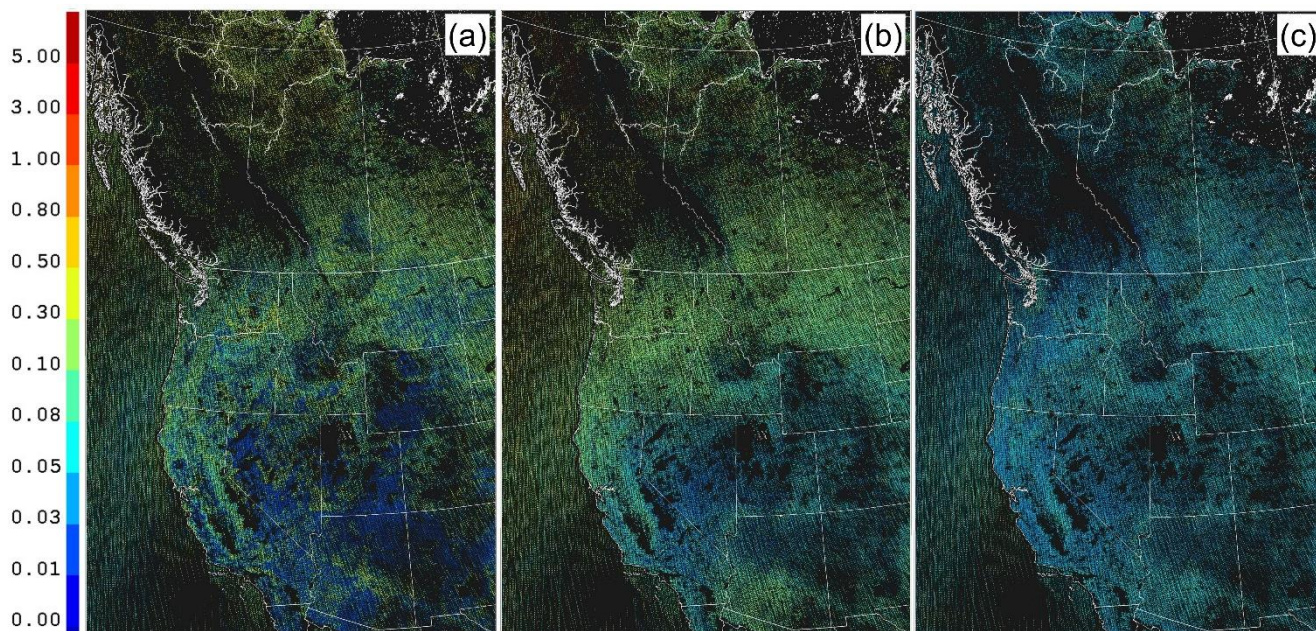
Figure 14: 550nm AOD comparison. (a) All MODIS observations sampled over the model domain and forecast duration and (b) GEM-MACH 2.5km simulation, driven by 10km GEM-MACH simulations, in turn driven by ECMWF Reanalysis for 2.5km domain boundary conditions. (c) GEM-MACH 2.5km simulation, driven by MOZART climatological boundary conditions.
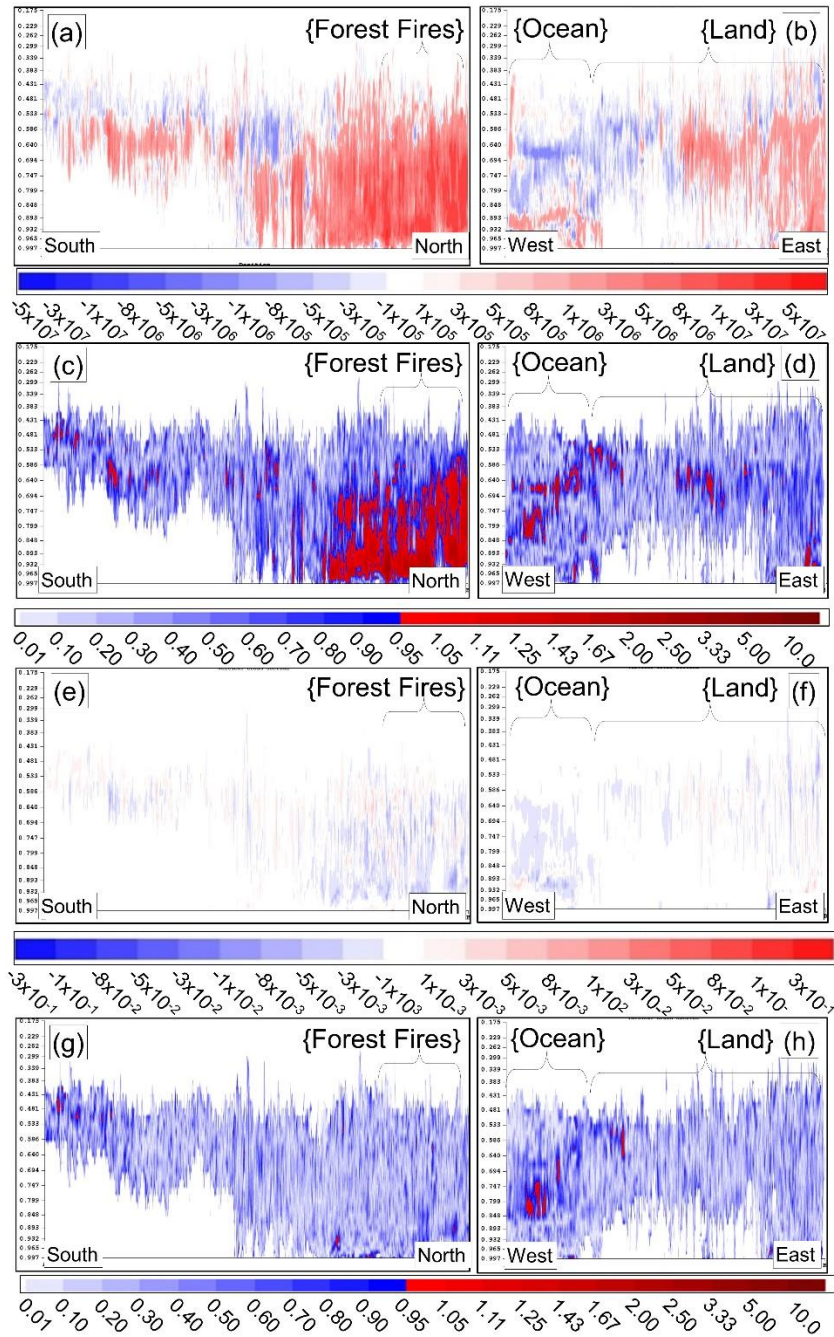
**Figure 15.** (a,b) Difference in mean (Feedback – No-Feedback) cloud droplet number simulations along south to north and east to west cross-sections through the middle of the model domain. (c,d) Corresponding significance level of mean cloud droplet number differences using the confidence ratio defined in equation (1) – red areas indicate ratio values greater than unity, i.e., significance at or above the 90% confidence level. (e,f) Difference in mean cloud droplet mass (g kg$^{-1}$) (g,h) Corresponding significance level of mean cloud droplet mass difference. *Note: the vertical axis in hybrid coordinates does not show all model levels for clarity; the model has much finer resolution in the lower part of the atmosphere than shown, and the portion of the vertical domain shown encompasses only the lower half of the levels in the model.*

1115
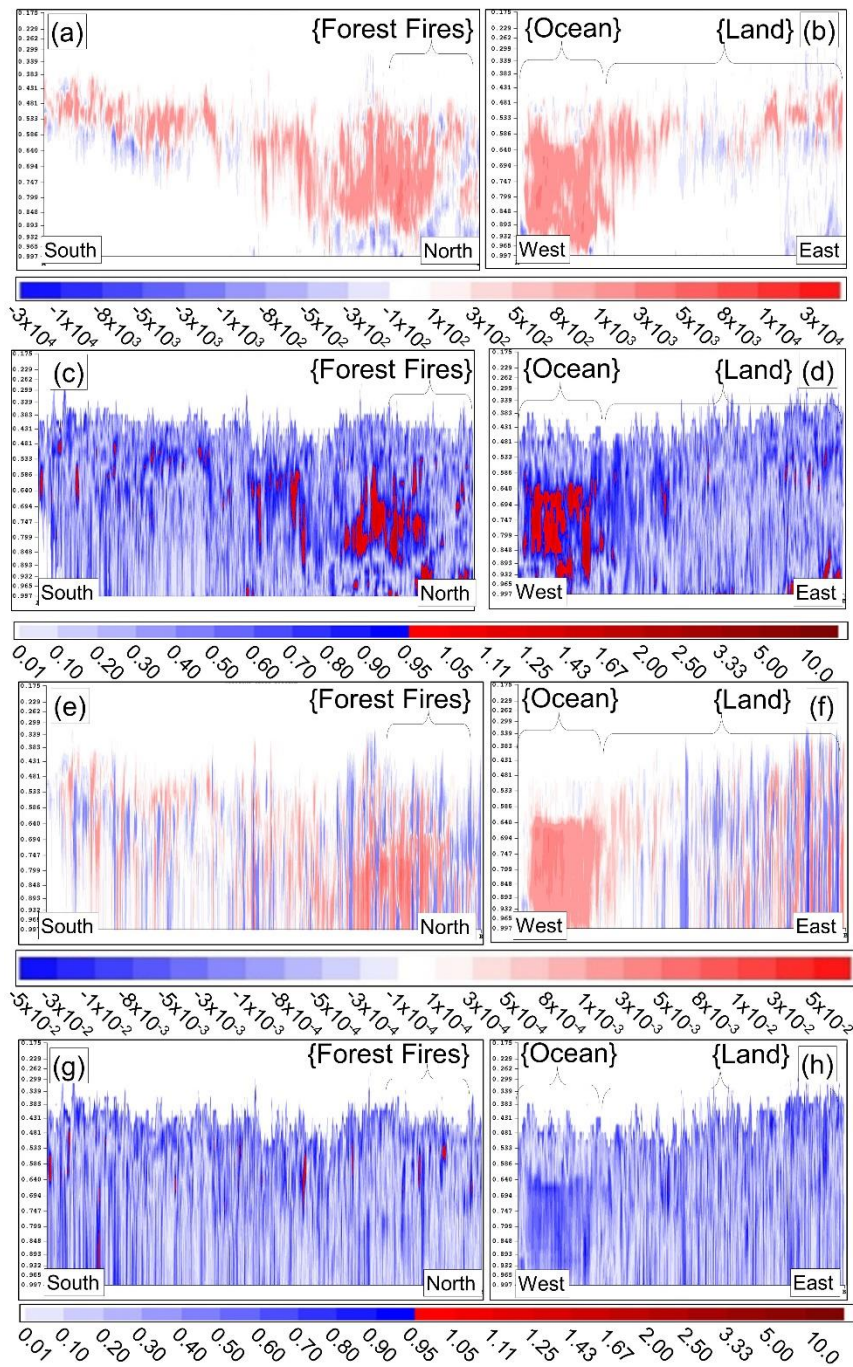


Figure 16. (a,b) Difference in mean (Feedback – No-Feedback) rain drop number simulations along south-to-north and east-to-west cross-sections through the middle of the model domain. (c,d) Corresponding significance level of mean rain drop number differences using the confidence ratio defined in equation (1) – red areas indicate ratio values greater than unity, i.e., significance at or above

the 90% confidence level. (e,f) Difference in rain cloud drop mass (g kg$^{-1}$) (g,h) Corresponding significance level of mean rain drop mass difference.
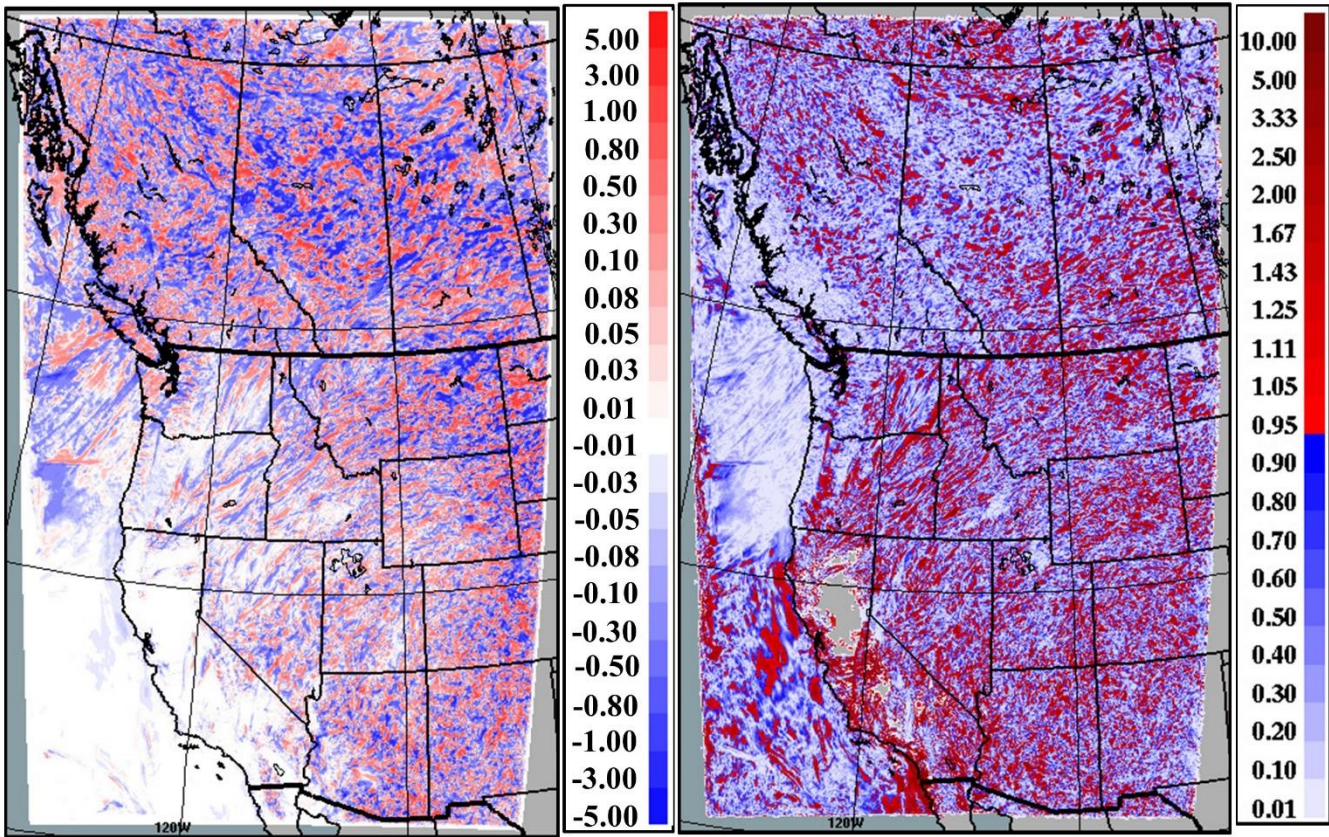


Figure 17: (a) Average (Feedback – No Feedback) total surface precipitation during the simulation period. (b) 90% confidence ratio – values greater than 1 indicate significantly different results at the 90% confidence level.
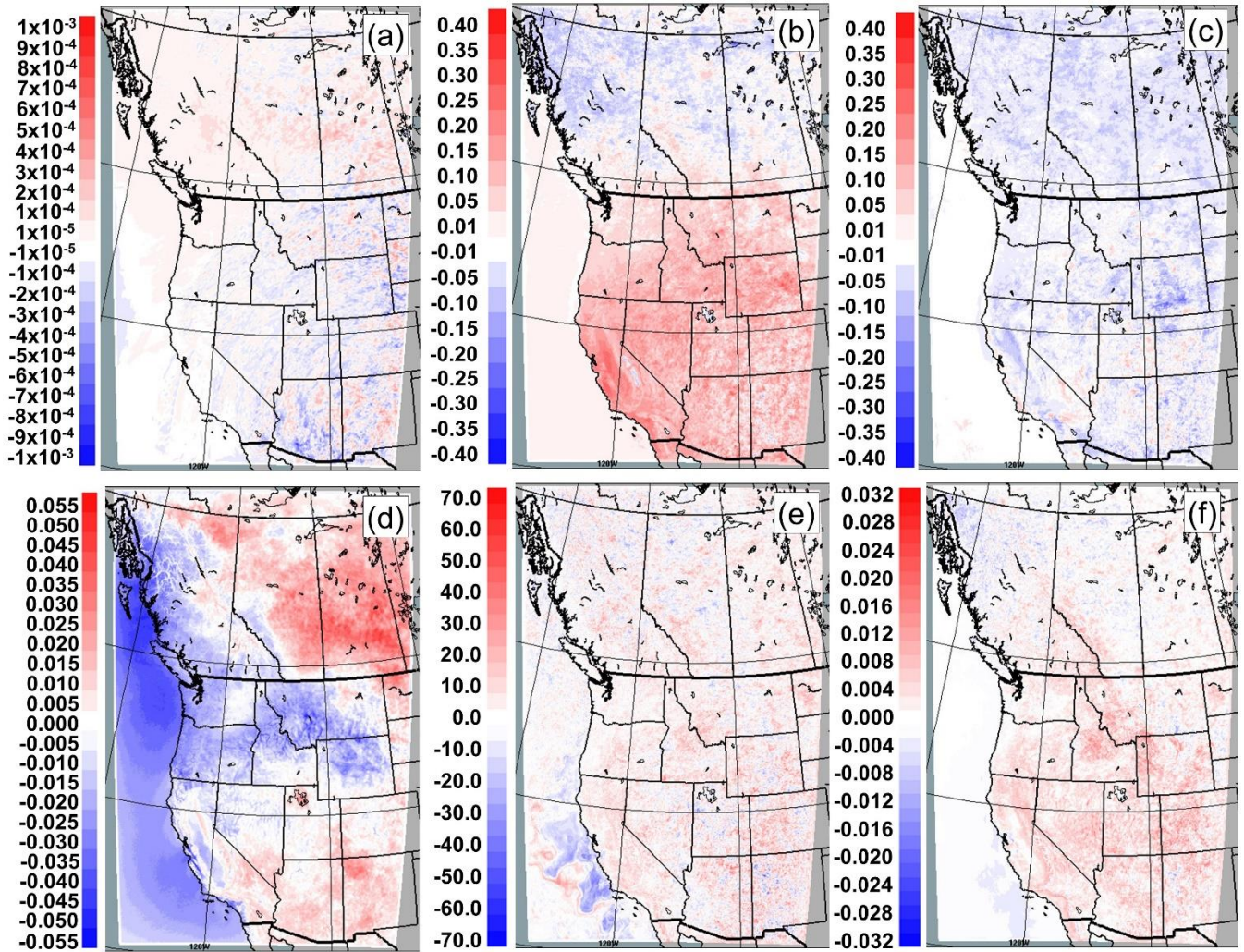
Figure 18: Differences in average meteorological fields (feedback – no-feedback; red values indicate more positive values in the feedback simulation than in the no-feedback simulation). Panels show average difference in: (a) specific humidity (g kg$^{-1}$); (b) air temperature (C), (c) dewpoint temperature (C), (d) surface pressure (mb), (e) planetary boundary layer height (m), (f) friction velocity (m s$^{-1}$).
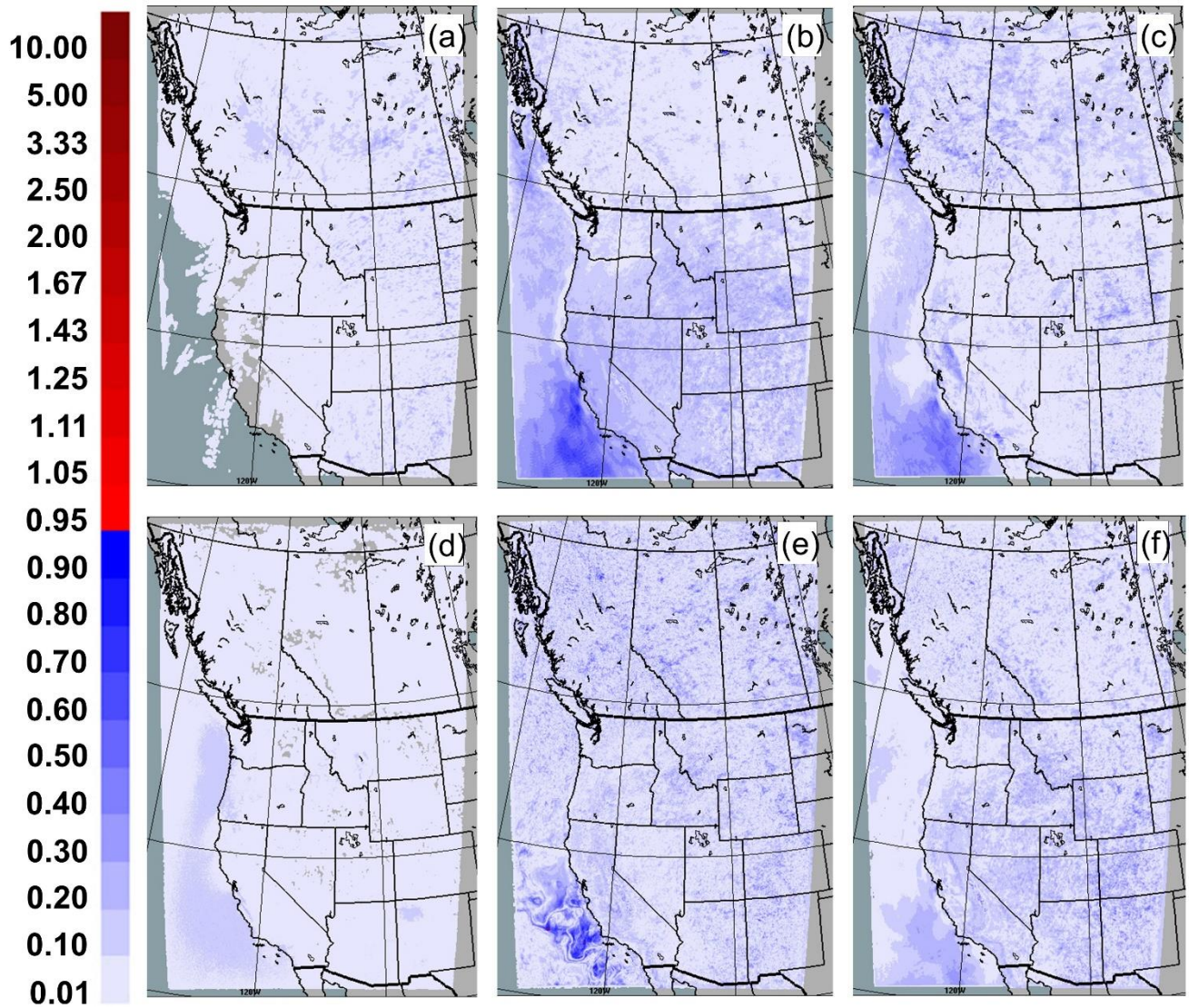
Figure 19: 90% confidence ratios, same fields as Figure 19. Values greater than 1 indicate significantly different results at or greater than the 90% confidence level.
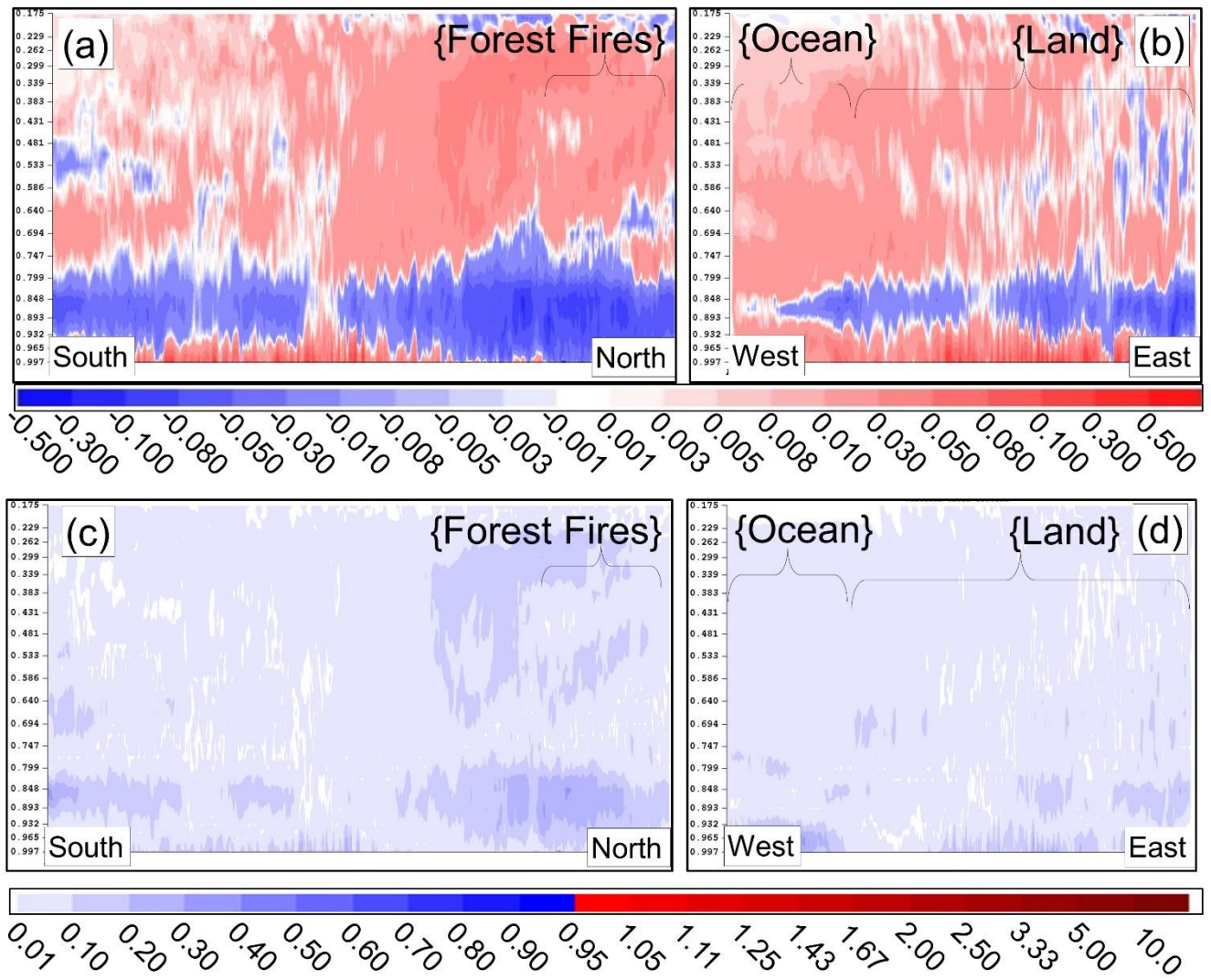
**Figure 20: (a,b)** Difference in mean (Feedback − No-Feedback) temperature simulations along south-to-north and east-to-west cross-sections through the middle of the model domain. **(c,d)** Corresponding confidence ratio of mean temperature differences − red areas indicate ratio values greater than unity, i.e., significance at or above the 90% confidence level.
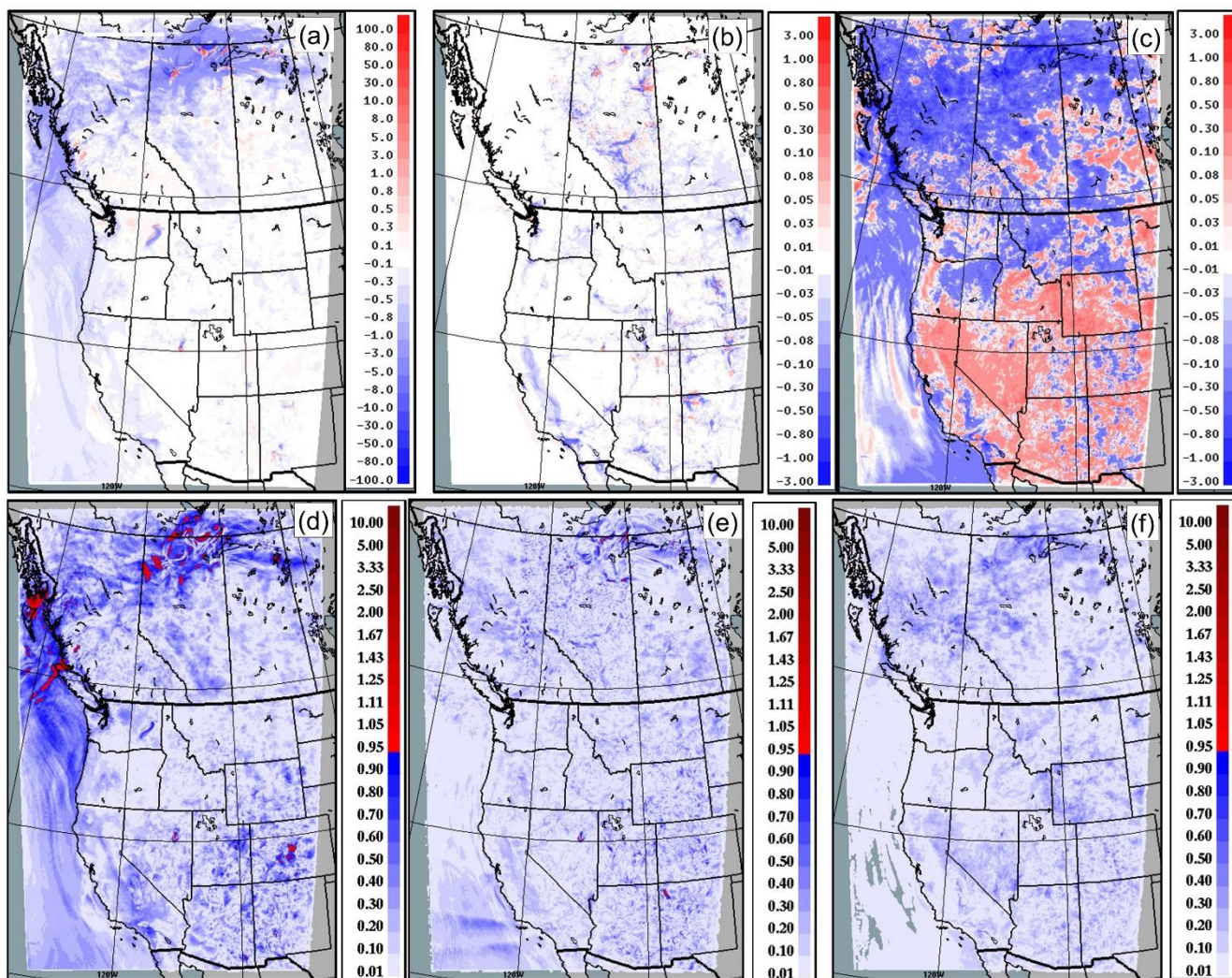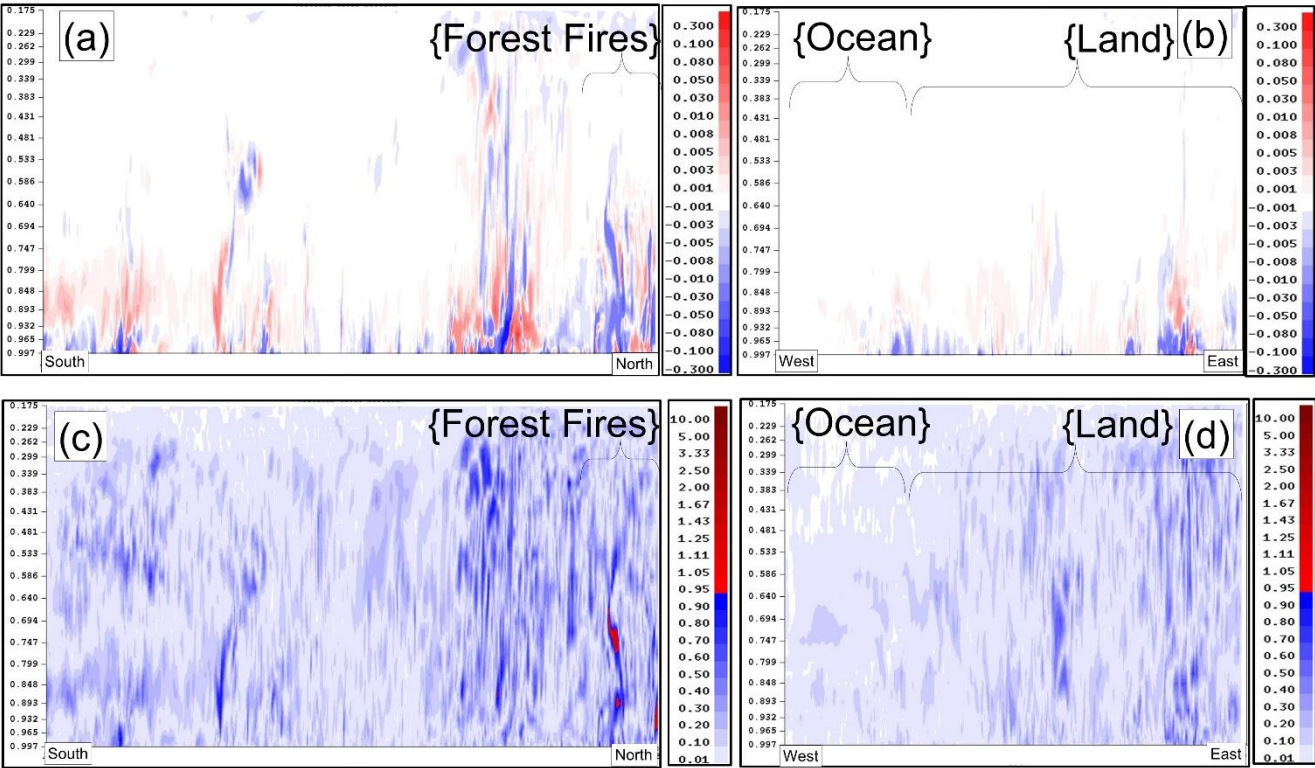
**Figure 21:** (a,b,c) Difference (Feedback – No-Feedback) in surface mean PM2.5 (ug m$^{-3}$), NO$_2$ (ppbv) and O$_3$ (ppbv), respectively. (d,e,f) Corresponding confidence ratio of mean differences – red areas indicate ratio values greater than unity, i.e., significance at or above the 90% confidence level.
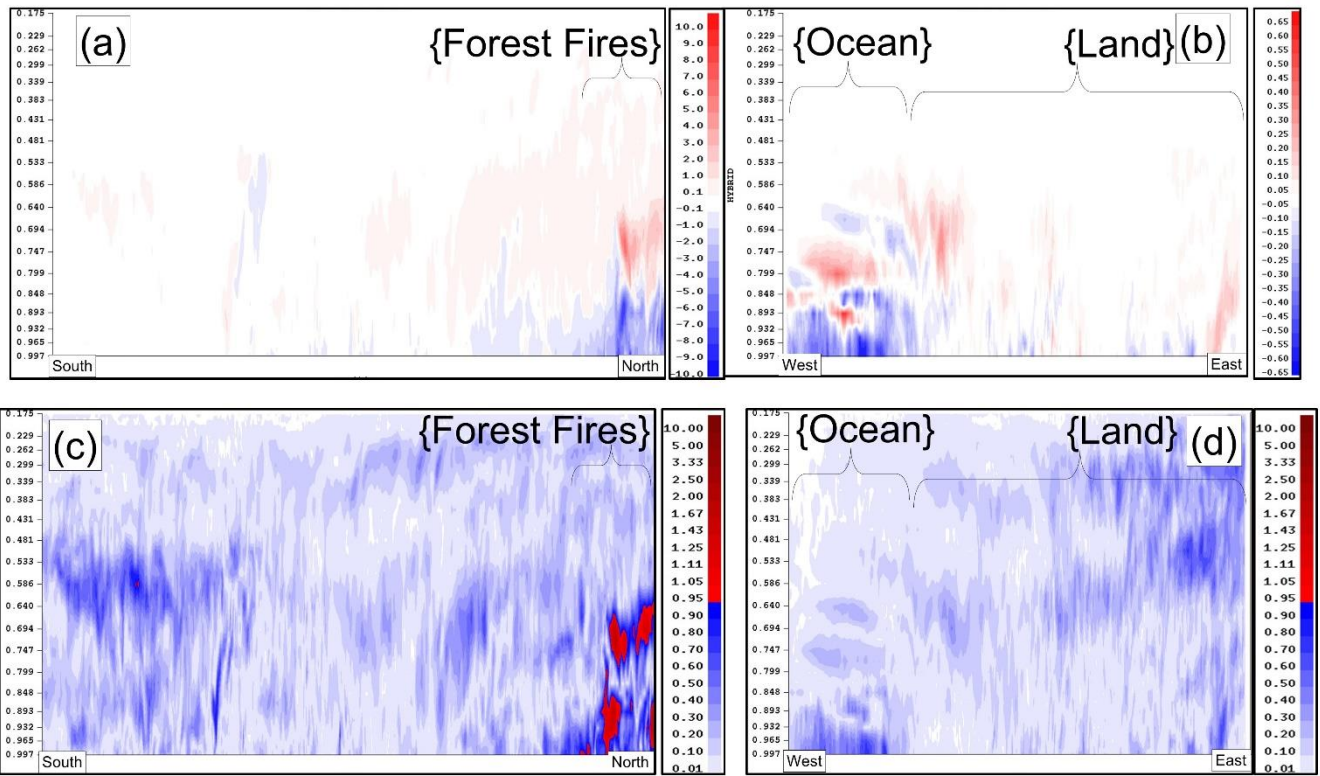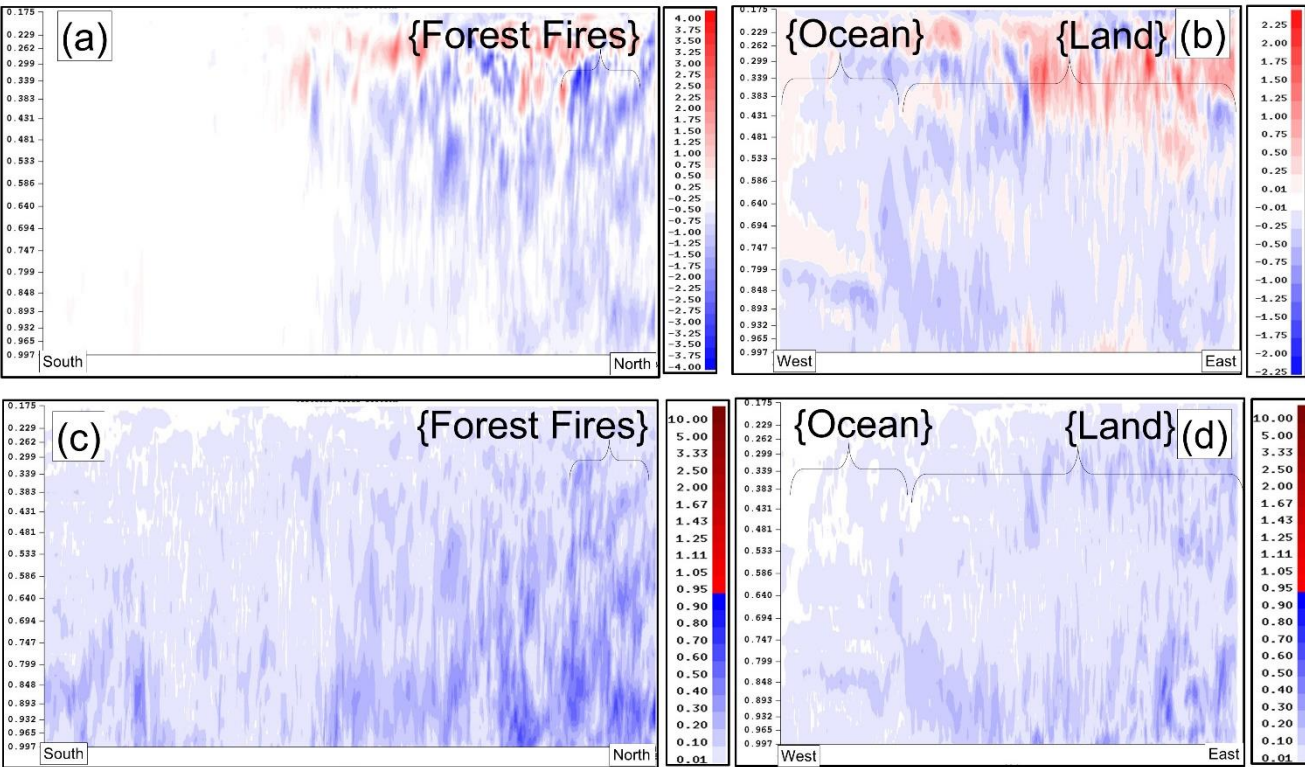
**Figure 22:** (a,b) Difference (Feedback – No-Feedback) in predicted mean PM2.5 (ug m$^{-3}$), along domain-center South-North and West – East cross-sections. (c,d) Corresponding confidence ratio of mean differences – red areas indicate ratio values greater than unity, i.e., significance at or above the 90% confidence level. Note that colour bar scales differ between (a) and (b).

Figure 23: (a,b) Difference (Feedback – No-Feedback) in predicted mean NO$_2$ (ppbv), along domain-center South-North and West – East cross-sections. (c,d) Corresponding confidence ratio of mean differences – red areas indicate ratio values greater than unity, i.e., significance at or above the 90% confidence level.

1162



1163
1164 Figure 24: (a,b) Difference (Feedback – No-Feedback) in predicted mean O₃ (ppbv), along domain-center South-North and West –
1165 East cross-sections. (c,d) Corresponding confidence ratio of mean differences – red areas indicate ratio values greater than unity,
1166 i.e., significance at or above the 90% confidence level. Note that colour bar scales differ between (a) and (b).
1167